Accepted Manuscript

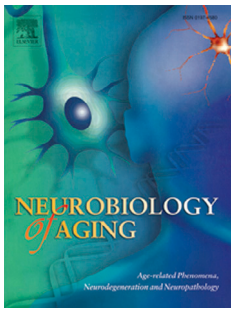

Age-related microstructural differences quantified using myelin water imaging and advanced diffusion MRI

T. Billiet, M. Vandenbulcke, B. Mädler, R. Peeters, T. Dhollander, H. Zhang, S. Deprez, B.R.H. Van den Bergh, S. Sunaert, L. Emsell

PII: S0197-4580(15)00160-8

DOI: 10.1016/j.neurobiolaging.2015.02.029

Reference: NBA 9231

To appear in: *Neurobiology of Aging*

Received Date: 29 October 2014

Revised Date: 26 February 2015

Accepted Date: 28 February 2015

Please cite this article as: Billiet, T, Vandenbulcke, M, Mädler, B, Peeters, R, Dhollander, T, Zhang, H, Deprez, S, Van den Bergh, B., Sunaert, S, Emsell, L, Age-related microstructural differences quantified using myelin water imaging and advanced diffusion MRI, *Neurobiology of Aging* (2015), doi: 10.1016/j.neurobiolaging.2015.02.029.

Age-related microstructural differences quantified using myelin water imaging and advanced diffusion MRI

Billiet, T[a,b,c,d], Vandenbulcke, M[d,e], Mädler, B[f,g], Peeters, R[b,d], Dhollander, T[c,h], Zhang, H[i], Deprez, S[a,b,c,d], Van den Bergh BRH[j,k], Sunaert S[a,b,c,d], L Emsell[a,b,c,d,e]

a. Translational MRI, Department of Imaging & Pathology, KU Leuven, Herestraat 49, Leuven 3000, Belgium.
b. Department of Radiology, University Hospitals Leuven, Herestraat 49, Leuven 3000, Belgium
c. Medical Imaging Research Center (MIRC), Herestraat 49, Leuven 3000, Belgium
d. Leuven Research Institute for Neuroscience & Disease (LIND), Herestraat 49, Leuven 3000, Belgium
e. Department of Old Age Psychiatry, KU Leuven, Herestraat 49, Leuven 3000, Belgium
f. Philips Healthcare, Philips Road 14, Hamburg 20099, Germany
g. Department of Neurosurgery, Medical Centre, University of Bonn, Sigmund-Freud-Straße 25, Bonn 53105, Germany
h. The Florey Institute of Neuroscience and Mental Health, Melbourne, Victoria, Australia
i. Department of Computer Science & Centre for Medical Image Computing, University College London, Gower Street, London WC1E 6BT, UK
j. Department of Psychology, Tilburg University, Tilburg 5000 LE, Netherlands
k. Research group on Health Psychology, KU Leuven, Tiensestraat 102, Leuven 3000, Belgium

Corresponding Author

First Name	Thibo
Last Name	Billiet
Highest academic degree	Master
Professional title	Ir.
Affiliation	• KU Leuven (Imaging & Pathology dpt. - Translational MRI unit), Leuven, Belgium • University Hospitals Leuven (Radiology), Leuven, Belgium • Medical Imaging Research Center • Leuven research Institute of for Neuroscience & Disease
Name and address for correspondence	Thibo Billiet Radiology, University Hospitals Leuven Herestraat 49 - box 7003 B – 3000 Leuven Belgium
Location of affiliation	Leuven, Belgium
Telephone number	+32 16 34 90 69
Fax number	+32 16 34 37 65
e-mail address	Thibo.billiet@uzleuven.be

Abstract

Introduction: Age-related microstructural differences have been detected using diffusion tensor imaging (DTI). Whilst DTI is sensitive to the effects of aging, it is not specific to any underlying biological mechanism, including demyelination. Combining multi-exponential T2 relaxation (MET2) and multi-shell diffusion MRI (dMRI) techniques may elucidate such processes.

Methods: Multi-shell dMRI and MET2 data were acquired on 59 healthy participants aged 17-70 years. Whole brain and regional age-associated correlations of measures related to multiple dMRI models (DTI, diffusion kurtosis imaging (DKI), neurite orientation dispersion and density imaging (NODDI)) and myelin sensitive MET2 metrics were assessed.

Results: DTI and NODDI revealed widespread increases in isotropic diffusivity with increasing age. In frontal white matter, fractional anisotropy (FA) linearly decreased with age, paralleled by increased 'neurite' dispersion and no difference in myelin water fraction (MWF). DKI measures and neurite density correlated well with MWF and intra- and extracellular water fraction (IEWF).

Conclusion: DTI estimates remain among the most sensitive markers for age-related alterations in white matter. NODDI, DKI and MET2 indicate that the initial decrease in frontal FA may be due to increased axonal dispersion rather than demyelination.

1. Introduction:

Throughout adulthood, the human brain undergoes significant biophysical changes in both white and grey matter (Pannese, 2011). In contrast to non-human primates, these maturating and regressive processes occur heterochronically in different brain regions (Haroutunian, et al., 2014).

Structural magnetic resonance imaging (sMRI) has played a pivotal role in the context of monitoring and understanding the healthy ageing process, for example, by measuring atrophy and detecting white matter (WM) lesions (Fjell, et al., 2009,Raz, et al., 1997,Salat, et al., 2009). However, single contrast sMRI is suboptimal for measuring microstructural changes, including myelination, which may predate atrophy (Haroutunian, et al., 2014).

Other MRI based techniques, such as those that are sensitive to the direction of water diffusion (diffusion MRI) or myelin content (relaxometry, magnetization transfer imaging) are increasingly being applied to study lifespan effects. The most widely used of these approaches is diffusion tensor imaging (DTI) (Basser, et al., 1994). Fractional anisotropy (FA) describes the degree of non-isotropic diffusion and is a popular, non-specific DTI metric that is used as a general indicator of microstructural status because of its sensitivity to changes in cell density, size, number and myelin status (Beaulieu, 2002,Beaulieu and Allen, 1994). See (Tournier, et al., 2011) for a review. Age-related differences in FA, mean diffusivity (MD), and radial diffusivity (RD) have been found in various WM regions. The changes are often non-linear (quadratic) with an initial increase in FA and decrease in MD and RD followed by a reversal that is frequently attributed to deficits in axonal membrane (myelin) integrity. The greatest changes are often found in the anterior corpus callosum (Bartzokis, et al., 2012,Brickman, et al., 2012,Davis, et al., 2009,Inano, et al., 2011,Lebel, et al., 2012,Pfefferbaum, et al., 2000,Salat, et al., 2005,Sullivan and Pfefferbaum, 2006).

Whilst DTI is a popular technique, it is not without significant limitations, many of which relate to the simplicity of the tensor model (Jones and Cercignani,

2010). In response, novel non-tensor based diffusion MRI techniques have been developed. In contrast to DTI, Diffusion Kurtosis Imaging (DKI) also measures non-Gaussian diffusion and may provide additional and complementary information to DTI (Jensen and Helpern, 2010,Jensen, et al., 2005). To date, only a few studies have applied this technique to study differences across the lifespan. In these studies, mean kurtosis (MK), a measure of tissue complexity was found to increase in WM during maturation and decrease in healthy aging (Coutu, et al., 2014,Falangola, et al., 2008,Gong, et al., 2014,Latt, et al., 2013).

Another advanced diffusion MRI analysis technique, neurite orientation dispersion and density imaging (NODDI)(Zhang, et al., 2012) aims to quantify the density and dispersion of neurites (i.e. axons and dendrites). These can be seen as independent factors influencing anisotropy and provide a more biologically intuitive model of diffusion changes. NODDI has been successfully applied in previous studies investigating pathological changes (Billiet, et al., 2014a,Lally, et al., 2014,Winston, et al., 2014) and neonates (Jelescu, et al., 2015,Kunz, et al., 2014,Melbourne, et al., 2013), but has not yet been used prospectively in healthy ageing.

Diffusion estimates have proven to be sensitive to many microstructural alterations, yet lack specificity. Furthermore, diffusion MRI cannot directly assess myelin, which has an important role in ageing processes. Several alternative MRI based techniques provide myelin markers, including the myelin water fraction (MWF) obtained from multi-exponential T2 relaxation (MET2, or "myelin water imaging, MWI"), and magnetization transfer imaging (MTI). Studies using MTI have found evidence of potential age associated demyelination; yet the lack of specificity of these measures for myelin means that MTI based findings need confirmation using alternative techniques. In this context, the MWF has superior specificity for myelin content (Stanisz, et al., 2004,Vavasour, et al., 2011). A few studies have been conducted assessing the evolution of myelination in neonates and children (Deoni, et al., 2012,Melbourne, et al., 2013,Whitaker, et al., 2008) yet limited information exists about the evolution of MET2 metrics during adulthood (Flynn, et al., 2003).

There are undisputable, heterogeneous WM microstructural changes associated with ageing as assessed using different MRI techniques. However, attributing differences in univariate MRI measures to specific microstructural features is confounded by a lack of specificity and, in the case of novel measures, a lack of studies characterising their behaviour in healthy tissue. In this multimodal MRI study we therefore aimed to quantify whole brain and regional age-related differences in both established (DTI) and novel diffusion MRI metrics (DKI, NODDI) as well as in the myelin specific MET2 technique in a prospective sample of healthy individuals. We contribute valuable normative data for future studies using these techniques and demonstrate the added value of using multiparametric MRI data for assessing age-related WM microstructural changes.

2. Materials & Methods

2.1 Participants

Age and gender matched healthy volunteers between the ages of 17 and 70 years old were recruited through local advertisement in the Leuven University Hospital. Inclusion criteria were the absence of current medical illness, diagnosis of a neurological or psychiatric disorder, previous brain surgery, traumatic brain injury, use of psychotropic medication, and contraindications to MRI scanning. The study was approved by the local Ethical Committee and conducted in accordance with the Declaration of Helsinki. Originally sixty-two volunteers participated of which fifty-nine were retained (min age: 17, max age 70). One dataset was discarded because of extensive white matter hyperintensities. The remaining participants were free of visible hyperintensities. Two datasets were discarded because of incomplete data acquisition. Participants were randomly scanned within a timeframe of 7 months, with the timing of data acquisition distributed evenly across the age-range studied. There were slightly more female participants than males (f/m = 36/23) but their mean age did not differ ($t = 0.49$, $p = 0.62$). There was no

significant difference in educational level across the age-range investigated (F= 1.68, p = 0.17). Education level in this instance refers to the highest educational qualification (i.e. most years of education) obtained in Belgium based on 5 levels, which include: primary school, secondary school (i.e. high school), higher education of short duration (equivalent to professional bachelor), higher education of long duration (equivalent to professional master) and university degree (academic bachelor + master).

2.2 Data acquisition

MRI brain scans were acquired using a 3T MR scanner (Achieva; Philips, Best, the Netherlands) and a 32-channel phased-array head coil.

2.2.1 Multi-exponential T2-relaxation

A 3D GraSE sequence was used to acquire multi-slice multi-echo data of the cerebrum in under 12 minutes (Maedler and MacKay, 2007,Prasloski, et al., 2012). The data consisted of 32 mid-axial slices for which 32 echoes were acquired with Δ TE = 10 ms (TE = 10, 20, …, 320 ms), TR = 1000 ms, EPI-read out factor of 3 and voxel size 1 x 1 x 2.5 mm^3.

2.2.2 Diffusion MRI

An echo-planar imaging (EPI), multi-shell, high angular resolution diffusion imaging (HARDI) scheme was used consisting of diffusion-weighted images for b-values of 700, 1000, and 2800 s/mm^2, respectively applied along 25, 40 and 75 uniformly distributed directions (Poot, et al., 2010). Each series of diffusion-weighted images was preceded by a b = 0 image. An additional 7 non-diffusion weighted images were acquired yielding 10 b = 0 images in total. Constant scan parameters were TR/TE = 7800 ms/90ms, 50 slices, voxel size 2.5 x 2.5 x 2.5 mm^3, parallel imaging factor 2.

A T1-weighted image was acquired for anatomical reference and image registration purposes using a whole brain 3D-TFE sequence consisting of 182

contiguous coronal slices with TE = 4.6 ms, TR = 9.6 ms, voxel size 0.98 x 0.98 x 1.2 mm^3. The total scan time of the protocol was approximately 45 minutes.

2.3 Data pre-processing

The main steps in the image-processing pipeline are visualized in Figure 1. Following data quality assurance and correction, the MET2 and diffusion parameter maps were calculated in each subject in native space. These parameter maps were then brought into a common template space via a series of controlled affine and non-affine registration steps. The datasets were masked to define which voxels should be included as WM (based on the T1-weighted anatomical image), and which should be excluded e.g CSF (including lateral ventricles), subcortical GM (including basal ganglia and thalamus) and the voxels closest to the cortical boundary. Parameter values were then assessed in each individual subject in masked template space. Each of these steps is described in more technical detail below.

2.3.1 Quality assurance & calculation of quantitative maps

Multi-exponential T2 relaxation

The T2 weighted volumes were visually checked for motion artifacts and in case of a blurred first echo image, the dataset was discarded.

A decay curve was obtained in each voxel from all T2 weighted images, and was transformed into a distribution of 120 mono-exponential T2 decay curves using regularized non-negative least squares estimation (Whittall and Mackay, 1989). We used the extended phase graph algorithm to account for possible stimulated echoes due to non-ideal refocusing pulse flip angles (Hennig, 1988,Prasloski, et al., 2011). A 1.02 regularization factor was used during the fitting procedure to assure smooth T2 amplitude distributions. From the T2 distributions the following MET2 metrics were derived on a voxelwise basis: myelin water fraction (MWF) was calculated as the area fraction between 10 and 40 ms relative to total T2 distribution area; intra- and extracellular water fraction (IEWF) as relative area between 40 and 200 ms; IEW-gmT2 is the geometric

mean T2 time of intra-and extracellular water; G-gmT2 is the geometric mean T2 time of the overall distribution. Example MET2 parameter maps are illustrated in Figure 2 and summarized in Table 1B.

Diffusion MRI

All DWIs were visually investigated by looping through each dataset in all three orthogonal views. Datasets with clear artifacts such as signal dropout, gross geometric distortion or bulk motion were discarded. Satisfactory datasets were corrected for eddy-current and motion-induced geometric distortions using the ExploreDTI toolbox, which is based on the approach described by Irfanoglu et al (Irfanoglu, et al., 2012). This step also included the appropriate reorientation of the B-matrix. (Leemans, 2009,Leemans and Jones, 2009). From the corrected and combined DWIs, diffusion tensors and diffusion kurtosis tensors were obtained per voxel(Jensen, et al., 2005), and the following parameters were derived: axial diffusivity (AD), radial diffusivity (RD), mean diffusivity (MD), fractional anisotropy (FA), axial kurtosis (AK), radial kurtosis (RK), mean kurtosis (MK) and kurtosis anisotropy (KA). NODDI metrics were derived using the NODDI toolbox[1]: neurite density index (NDI), orientation dispersion index (ODI) and (Gaussian) isotropic fraction (FISO). Example dMRI parameter maps are illustrated in Figure 2 and summarized in Table 1.

2.3.2 Image registration

The registration pipeline is illustrated in Figure 1. A population-based template was constructed based on the b=2800 shell of the diffusion MRI dataset, using an affine and subsequently non-rigid DTI-based registration algorithm incorporating tensor reorientation (Leemans and Jones, 2009,Van Hecke, et al., 2007). The b = 2800 shell was chosen for optimal angular contrast. All parameter maps were computed in native space and then coregistered to this population-based template using the following steps. First, the "Advanced Normalisation Tools" (ANTS) toolbox (Avants, et al., 2008) was used to affinely register the MET2 metrics to the native T1 image by maximization of mutual

[1] http://www.nitrc.org/projects/noddi_toolbox

information between the first echo image and the T1 image. Affine transformations were justified by the absence of any geometric distortions in MET2 data. Next, the MET2 metrics and T1-based tissue classes were diffeomorphically registered (Avants, et al., 2008) to b = 1000 data (for optimal GM and WM tissue contrast). To optimally account for remaining geometric distortions of dMRI data, two similarity measures with equal weight were used: mutual information between the T1 image and average of the b=1000 DWIs, and cross correlation between T1 WM and the FA image. Finally, all the MET2 as well as WM tissue segmentations, DTI, DKI and NODDI native parameter maps were nonrigidly normalized to the group template using an affine and non-rigid DTI-based coregistration algorithm (Leemans and Jones, 2009,Van Hecke, et al., 2007).

2.3.3 Construction of white matter masks

To reduce partial volume effects, each participant's image was multiplied by a WM mask based on their individual thresholded (0.8) and binarised WM tissue map obtained from the SPM8 segmentation of their native T1 image. As such, we restricted analysis to voxels containing at least 80% WM. Furthermore any voxels that overlapped with the "Automatic lateral ventricle delineation" (ALVIN) ventricle mask were excluded (Kempton, et al., 2011). Additionally, another WM mask was applied based on the average white matter segmentation of all subjects, thresholded at 0.8 and binarised. This was done to ensure that only voxels that had a high likelihood of being WM in all participants were incorporated. Finally, to reduce partial volume contamination from voxels in the basal ganglia and thalamus regions, an exclusion mask was applied including caudate, putamen, globus pallidus and thalamus ROIs as defined by the Harvard-Oxford cortical and subcortical structural atlas (Frazier, et al., 2005). The final mask is visible in Figure 1 and in more detail in Supplementary Figure 1 and 2.

2.4 Data analysis

2.4.1 Region-of-interest analysis

For assessing the correlation of all metrics with age in well-defined regions of interest (ROIs), we used the Johns Hopkins University (JHU) WM atlas labels (Mori, et al., 2005). For each participant, the mean metric value of voxels inside a ROI was calculated, excluding the lowest 2% and highest 2% of values. Because the 3D GraSE sequence has a limited FOV, metrics were only evaluated in those regions for which all participants had data in more than half of the ROI (i.e. all brainstem and cerebellum regions were excluded). To reduce multiple comparisons, the analysis combined bilateral structures into single regions (n=23). This was deemed acceptable because age-related differences have been shown to occur predominantly bilaterally (Callaghan, et al., 2014,Draganski, et al., 2011,Lebel, et al., 2012,Salat, et al., 2005). Also small ROIs (mean – standard deviation less than 100 voxels) were excluded from the analysis to avoid ROI size bias. These included the tapetum, uncinate fasciculus, superior fronto-occipital fascicles, the cingulum near the hippocampus (separate from the cingulum near the cingulate gyrus) and the fornix body (separate from the larger fornix crescent/stria terminalis). The remaining ROIs and their size in voxels are summarized in Supplementary Table 1.

The resulting mean metric values inside ROIs and whole cerebrum WM were then assessed for their linear and quadratic correlation with age and the shared variance between any two metrics was computed. Correlations were deemed significant if the resulting p-value was below 0.05 after correcting for multiple comparisons using the Holm-Bonferroni method for family-wise error (FWE). The Steiger z-test was applied to assess whether there was a significant difference ($p_S<0.05$) between linear and quadratic correlation with age for each ROI and metric.

2.4.2 Voxel-wise analysis

Statistical analyses were carried out on smoothed parameter maps (FWHM=6mm) in population atlas space using mass-univariate linear regression as embedded in the general linear model framework of SPM8 (statistical parametric mapping software;

http://www.fil.ion.ucl.ac.uk/spm/software/spm8/, London, United Kingdom) with age as a regressor. 2-tailed t- tests were used to look for differences in 15 MRI-based measures with age: DTI metrics (FA, MD, AD, RD), DKI metrics (KA, MK, RK AK), NODDI metrics (NDI, ODI, FISO) and MET2 metrics (MWF, IEWF, IEW-gmT2, G-gmT2). An explicit mask limited the analysis to the average WM mask also used in ROI analysis (i.e. average of WM tissue maps thresholded at 0.8, binarised and excluding basal ganglia, thalamus and lateral ventricles).

Additionally, we performed a voxel-based morphometry analysis using "diffeomorphic anatomical registration through exponentiated Lie algebra" (DARTEL) (Ashburner, 2007), investigating the correlation of WM volume with age, expressed as a T-score. This was performed on smoothed (FWHM = 6mm) modulated normalized WM maps in MNI space generated from the standard SPM8 DARTEL pipeline. Total WM was calculated using the SPM get_totals script[2].

In all SPM analyses, family-wise error was controlled using an FWE threshold of p=0.05 and clusters surviving this threshold were deemed significant below p_{FWE}=0.05 at cluster-level.

3. Results

3.1 Region-of-interest analysis

Figure 3 illustrates the linear correlation of DTI, DKI, NODDI and MET2 metrics with age in WM regions and in the cerebral WM (mask). ROIs and metrics are ranked according to the mean shared variance (R^2) with age. Regions are ranked from top to bottom according to average shared variance across metrics. Results for the total cerebral WM are added on top of the figure for comparison. Metrics are ranked from left to right according to average R^2 across ROIs. Figure 4 illustrates the correlation coefficient (i.e. square root of shared variance) for quadratic fit. A positive sign means the metric vs. age relationship

[2] http://www0.cs.ucl.ac.uk/staff/G.Ridgway/vbm/get_totals.m

(a parabola) resembles a U-shaped curve while negative coefficients indicate an inverse U-shaped curve.

3.1.1 Regional correlations

On average across regions, the NODDI measure of isotropic diffusivity (FISO) showed the largest differences with age, followed by neurite dispersion (ODI) and fractional anisotropy (FA). In some regions, a quadratic correlation describes the data significantly better than a linear correlation. These region-metric combinations are denoted with a black cell border in Figure 4. As an example the curves of RD, MK, ODI and IEWF in selected ROIs are illustrated in Figure 5.

The ROIs that show the strongest correlation with age on average across metrics were the fornix, cerebral peduncles, external capsules and the genu of corpus callosum. The least strong correlations were found in posterior regions, including the callosal splenium.

3. 1. 2 Diffusion metric correlations

The NODDI metrics were frequently positively correlated with age across the regions investigated. FISO showed the highest correlation with age in the external capsules ($r = 0.67$, $p_{FWE} < 0.001$) followed by the total cerebral WM ($r = 0.62$, $p_{FWE} < 0.001$), suggesting more free (isotropic) diffusion with age. This is also reflected in the positive correlations of MD (in cerebral WM: $r = 0.31$, $p_{FWE} = 0.005$). Figure 4 shows that age-related differences of FISO and all diffusivities (MD, RD, AD) tend to express a U-shaped pattern, which means a local minimum is reached after which values increase. The sagittal stratum is the only region where RD and MD show a significantly better quadratic, compared to linear fit.

Because ODI and NDI are believed to represent independent aspects of FA (Zhang, et al., 2012) we group results from these metrics here. In most ROIs, ODI and FA show similar but opposite linear correlation, suggesting reduced anisotropy with increasing age. Figure 4 reveals that in most ROIs where both FA and ODI change significantly, the curves of ODI vs. age and FA vs. age are opposite to each other, indicating some similarity between both. The

(predominantly linear) positive correlation of NDI with age furthermore reflects increasing intracellular-like signal relative to the extracellular-like signal. The profiles of FA, ODI and NDI vs. age were not consistently U-shaped or inverse U-shaped across regions.

Diffusion kurtosis metrics revealed less age-related differences compared to DTI and NODDI metrics. Of all the DKI parameters, AK displayed the most significant correlation with age, reflected by increasing values over the lifespan. Mean kurtosis increased most significantly in the anterior limb of the internal capsules ($r = 0.50$, $p_{FWE} = 0.012$) and presented inverse U-shaped profiles. Differences in RK and KA were too small to reveal the shape of quadratic fitted curves, as only few ROIs yielded above threshold correlation coefficients.

3.1.3 MET2 metric correlations

Compared to diffusion MRI metrics, the differences in MET2 metrics were generally smaller. The most significant differences in MET2 metrics were found in the fornix crescent/stria terminalis. In this structure MWF showed a trend towards a linear increase ($r = 0.46$, $p_{FWE} = 0.057$) and IEWF decreased with age as a U-shaped curve ($r = -0.56$, $p_{FWE} = 0.0074$).

3.2 Voxelwise assessment of lifespan effects

3.2.1 Whole brain correlations

There was no significant correlation between total WM volume and age (linear: $r = -0.0094$ ($p = 0.94$), quadratic: $r = -0.0034$ ($p = 0.98$)). Results from our voxel based morphometry DARTEL analysis additionally revealed no statistically significant regional WM volume effects at the selected cluster-level threshold of $p_{FWE}=0.05$.

3.2.2 Diffusion MRI metrics

DTI

Figure 6 illustrates regional differences in FA, MD, RD and AD. Effects were widespread including a bilateral anterior reduction in FA located along the

frontal projections of the corpus callosum (T>5.28, p_{FWE} <0.009 at cluster-level). This decreased anisotropy was mainly paralleled by an increase in RD (T>5.48, p_{FWE}<0.01 at cluster level) and less by MD or AD. Anisotropy was decreased and (mainly radial) diffusivity increased in superior parietal WM (corona radiata) and regions of crossing fibres such as the centrum semiovale (FA: T = 7.17, p_{FWE} < 0.001; RD: T = 7.41, p_{FWE} < 0.001).

DKI

Figure 7 illustrates regional differences in AK, MK, RK and KA. There were substantially fewer age-related differences detected using DKI compared to DTI. Similar to MD, MK increased with age in the corona radiata (T=7.40, p_{FWE}<0.001). In contrast to DTI where RD appeared to drive the increased mean diffusivity, MK was more paralleled by an increase in AK (T = 7.42, p_{FWE} < 0.001) than RK (T = 6.44, p_{FWE} = 0.001). The internal capsules furthermore showed a trend towards increasing MK (T=4.25, p_{FWE} = 0.022)

NODDI

Figure 8 illustrates regional differences in FISO, ODI, and NDI. The most significant effects were widespread increases in FISO throughout most of the cerebral WM, including the corpus callosum body and corona radiata, but with only limited increases in the occipital lobe.

Of the NODDI metrics, differences in NDI were smallest, with increases in the posterior corona radiata. Only very limited differences in NDI were found in WM of the frontal lobe.

ODI on the other hand expressed widespread linear increases with age including both anterior and posterior corona radiata, the intersection of several parietal and occipital fiber pathways, (T = 7.84, p_{FWE}<0.001) and posterior thalamic radiation (T= 5.82, p_{FWE}<0.001).

3.2.3 Myelin water imaging metrics

Figure 9 illustrates regional differences in MWF, IEW-gmT2 and G-gmT2. Overall, age-related differences were minor and only few results were significant. Mean T2 time (G-gmT2), IEWF and IEW-gmT2 slightly decreased in the external capsules (T = 5.76-6.27, p_{FWE} = 0.001 – 0.004)
There was a trend towards an overlapping increase in MWF and decrease in IEWF and G-gmT2 (but not IEW-gmT2) in the midbrain (T = 4.22 – 5.39, p_{FWE}= 0.012 - 0.23). Minor increases of all MET2 metrics were found in the corona radiata and of IEW-gmT2 in frontal WM. Notably, unlike with the diffusion metrics, MET2 metrics displayed both increases and decreases *within* metrics, which may reflect changing T2 properties of tissue over the lifespan.

3. 3 Correlation between metrics

Figure 10 displays the shared variance (i.e. the square of the linear correlation coefficient) between pairs of metrics in whole cerebral WM illustrating how much similar or unique information the different metrics provide.

As expected, DTI metrics have a high proportion of shared variance among themselves (i.e. intra-modal). The same is true for DKI and MET2, while NODDI metrics share only limited variance with each other (FISO vs. ODI: 12%, NDI vs. ODI: 3%, FISO vs. NDI: 21%). FISO, being an indicator for isotropic diffusivity, correlated strongly with MD (31%), RD (30%) and AD (20%), which also quantify isotropic diffusion. Across whole cerebral WM, the measures of anisotropy FA and ODI showed rather strong (negative) correlations with each other resulting in 36% of shared variance. In contrast, NDI was not significantly correlated with FA (17%) or ODI (3%). MWF and IEWF correlated strongly with DKI metrics and NDI, but not with DTI measures. Similarly, NDI showed higher shared variance with DKI metrics (in particular with MK: 89%) than with DTI metrics.

4. Discussion

4.1 Summary

In this cross-sectional study, we examined the relationship between multiple diffusion MRI and myelin-sensitive MET2 "myelin-water imaging" measures and age in brain WM in a healthy adult population. We used complementary ROI and voxel-based analyses, and examined the relationships between the different parameters used in these analyses. Our results indicate widespread WM microstructural differences in the absence of gross WM atrophy, with heterogeneous regional alterations between different measures, potentially reflecting different aspects of microstructural change and their evolution over the period of late development and early ageing. Metrics quantifying Gaussian diffusivity (in particular FISO) had the strongest correlations and most widespread age-effects, possibly related to cerebrospinal fluid increase, whilst non-DTI metrics correlated well with myelin water imaging measures.

4.2 Study findings in the context of retrogenesis and (de)myelination

Our results are in agreement with previous findings of an age-related decline in FA that is more pronounced in frontal regions (Bartzokis, et al., 2012,Davis, et al., 2009,Lebel, et al., 2012,Salat, et al., 2005) and which may reflect an anteroposterior gradient of retrogenesis (Bartzokis, et al., 2012,Inano, et al., 2011,Kumar, et al., 2013,Lebel, et al., 2012,Madden, et al., 2004,Pfefferbaum, et al., 2000,Salat, et al., 2005). In this process, WM fibers that were myelinated latest during development (e.g. genu of corpus callosum) have thinner myelin sheaths than early developing WM (e.g. splenium of corpus callosum) and therefore degenerate first during late adulthood and senescence.

Although controversial (Wheeler-Kingshott and Cercignani, 2009), changes in RD have been associated with changes in the myelin sheath (Song, et al., 2005). The age-related decrease in FA and increase in MD we detected were indeed accompanied by a more significant increase of RD than AD suggesting a myelin-related contribution to FA decrease. However, our results from myelin water imaging run somewhat counter to the demyelination hypothesis as we

detected positive, not negative linear correlations between age and MWF, in agreement with Flynn et al. (Flynn, et al., 2003). The low shared variance between MWF and FA in our study indicates that age-related FA changes do not necessarily correspond to changes in myelin content. This is in line with previous (non-aging) findings showing little correlation between FA and myelin measures (Beaulieu, 2002,Beaulieu and Allen, 1994,De Santis, et al., 2014,Madler, et al., 2008). Furthermore, other metrics that are sensitive for tissue fractions (IEWF, NDI) or compartmentalization (kurtosis metrics) did not show large age-related differences in frontal WM.

This begs the question of what actually drives the decrease in frontal FA, if it is not demyelination. Figure 8 has shown us a frontal increase in neurite dispersion (ODI) as modeled by the NODDI framework. Moreover, throughout the WM, ODI shared 36% of variance with FA (Figure 10). Although highly speculative, these combined findings suggest that rather than demyelination or alterations in tissue compartmentalization, increased axonal disperion may drive the earliest decreases in frontal FA. In line with this argument, a study investigating the correlation of similar (but not the same) MET2 and multi-shell dMRI metrics in a young cohort (mean age/standard deviation = 24.2/2.8 yrs) found that DTI measures are more dependent on the underlying microarchitectural paradigm (e.g. presence/number of crossing-fibers) than metrics based on multicompartment models (De Santis, et al., 2014).

4.3 Kurtosis metrics and NDI may reveal signs of late maturation.

The VBA and ROI results finding positive correlations of age with MK and RK diverge from previous studies in which negative correlations were found (Coutu, et al., 2014,Gong, et al., 2014,Latt, et al., 2013). Age-related differences in AK were only reported in (Coutu, et al., 2014) and in contrast to our findings showed negative correlation with age. This could be explained by the older sample in the Coutu et al. study, which may have captured the phase of decline while our sample reflects late maturation and early ageing. Figure 4 indeed suggests that AK and MK in most ROIs follow an inverted U-shaped curve which, given the positive linear correlation with age (Figure 3), goes along with an

initial increase (associated with ongoing maturation) and subsequent decline. In DTI metrics on the other hand, the phase of reversal seems to have already passed, as FA continues to decrease (inverted U-shape) and diffusivities continue to increase (U-shape). DTI and DKI metrics may therefore relate to different dynamics throughout the lifespan, meaning DTI metrics may reveal early decline through the linear correlation coefficients, while kurtosis metrics may capture signs of late maturation.

Similar to kurtosis metrics, we detected an increase of NDI with age instead of an expected decrease. The pattern of age-related differences of NDI closely resembled that of kurtosis metrics, with the largest clusters in superior parietal WM (Figures 7,8) and a trend towards an inverted U-shape curve in total cerebral WM (Figure 4). Furthermore Figure 10 has shown that NDI and MK correlate very strongly and have 89% of shared variance, suggesting a common driving factor. One possible explanation could be that age-related differences in non-Gaussian diffusion as measured by MK are largely driven by changes to axonal density.

4.4 MET2 metrics are less sensitive to age-related differences during early to mid-adulthood than diffusion measures

As only minor differences with age were found using MET2, it may be less suitable for studying early aging effects than diffusion MRI and DTI and NODDI metrics in particular. While shared variance values between MET2 and DTI metrics were below the significance threshold (Figure 10), some degree of similarity was detected between MET2, DKI and NDI. This similarity is not surprising as kurtosis is believed to reflect the degree of compartmentalization (Hui, et al., 2008), which is also reflected in MWF, IEWF and NDI.

Interestingly, in ROIs where differences in MWF were detected, the correlation with age was positive, suggesting an increase in myelin content with age. Although in agreement with Flynn et al. (Flynn, et al., 2003), this is counterintuitive. In this context it is important to keep in mind that MWF and IEWF are defined as a ratio relative to the total visible T2 distribution. An age-related increase in MWF may therefore also be explained by an absolute loss of

IE water. An age-related decrease of MWF may indicate both demyelination and also an absolute increase of IE water or the presence of an additional water pool with T2 values outside both myelin and IE integration windows (i.e. between 200ms and 2s). The latter is unlikely to be present in the current study sample as they have only been detected in pathologic white matter, e.g. in case of phenylketonuria (Laule, et al., 2007b) or multiple sclerosis (Laule, et al., 2007a).

4.5 Comparison between ROI and VBA results

The advantage of an ROI analysis for aging studies is that results can easily be localized to certain specific anatomical regions and the number of statistical comparisons may be reduced relative to whole brain VBA approaches. Moreover, the introduction of smoothing and statistical thresholds means that changes in smaller regions such as the fornix, are less readily detected using VBA. One would expect however, that the greatest regional changes would be detected by both methods. Indeed, in most regions, results from our VBA and ROI analysis are in agreement. There were however some exceptions. For example, in the posterior corona radiata, VBA detected subtle differences in MET2 metrics, MD and AD that were not detected in the ROI analysis. This could be due to ROIs not capturing as much WM in this region as well as differential partial volume effects, smoothing, and statistical significance thresholds related to FWE correction.

4.6 Methodological considerations

Our results are largely in accordance with previous MRI findings on larger populations and neurobiology. The age range of our participants most likely captures the processes of late development and early neurodegeneration, and therefore our findings may be less comparable to studies that include younger or older participants. For example, analyses including participants over and under 60 years old have demonstrated more significant decline in the older group (Salat, et al., 2005). This could also explain why we did not find any significant decrease in WM volume with age, and why some parameters did not display a

quadratic correlation with age. Because WM volume (and also grey matter volume) did not decrease significantly, we did not include brain volume as a covariate. This could also account for discrepancies with other studies.

Undertaking a multimodal multiparametric analysis such as in this study necessarily requires multiple image registration steps. In order to minimize registration errors, we used a population atlas based approach and sophisticated well-validated non-linear registration methods (Avants, et al., 2008), and assessed registration accuracy at each stage of the processing and analysis pipeline. However, as with all studies of this type, we cannot rule out the contribution of subtle registration, interpolation and partial volume effects to our findings (Van Hecke, et al., 2011,Vos, et al., 2011). In this context, although we did not detect voxel-wise correlations between age and WM volume, it is still possible that the associations we have detected reflect age-related macrostructural changes rather than changes in specific microstructural elements such as myelin content.

Some metrics in our study varied with age, however, correlation does not imply a causal relationship. Other factors that are not related to age such as IQ may have an influence on these metrics. We did not explicitly test IQ in this sample; however, there were no differences in educational level across the age-range studied. Participants of different ages were also randomly scanned, reducing the influence of scanner changes over time.

In vivo MRI metrics are indirect measures based on averaging multiple tissue properties over voxels many times larger than the structures that are being probed. Whilst the various metrics are described in terms of biological properties such as intra and extracellular water, or myelin, in reality these labels are based on mathematical models as applied to imperfect MRI data. We detected a number of counterintuitive findings in this context. For example, NDI (reflecting neurite density), increased with age. This highlights the need for further basic research into the neurobiological correlates of diffusion MRI and MET2 measures as the models are influenced by other tissue properties beyond

those the metrics attempt to characterize. For example, WM regions in the deep WM and the midbrain are close to structures that contain iron or accumulate iron with age (Callaghan et al, 2014). Iron influences the T2 relaxation signal, which underlies all the metrics assessed in this study.

5. Conclusion

Using advanced diffusion MRI and multi-exponential T2 relaxation we found age-related differences in multiple MRI measures of microstructure across the brain WM that predate atrophy. Commonly reported frontal WM decreases in FA may not reflect demyelination, but an increase in axonal dispersion. The correlation between MET2, DKI metrics and neurite density (NDI) suggests they may be sensitive to similar microstructural features, whilst DTI and NODDI appear to be most sensitive to lifespan effects in young to mid-adulthood.

Further research into the underlying biological basis of novel MRI based measures is required, however this study clearly demonstrates the added value of using multimodal multiparametric MRI data for assessing age-related WM microstructural differences.

Acknowledgements.

The authors would like to thank Frederik Dekeyzer for valuable discussions on statistical theory, Marjolein Verly for help with scanning and all our volunteers for their participation.

This research was supported by funding from the European Union Seventh Framework Programme under grant agreement 279281 (TB, BVdB), KU Leuven, PFV/10/008 grant (LE, MV, SS) and KU Leuven international mobility bursary (LE).

Disclosure statement

The authors have no actual or potential conflicts of interest.

Figure and table legends

Figure 1.

Image processing pipeline used in the current study. Aff. = Affine, Diff. = diffeomorphic, MI = mutual information, CC = cross correlation, NR = non-rigid.

Figure 2.

Parameter maps obtained from a single participant in template space. FA: fractional anisotropy; MD: mean diffusivity (mm^2/s); RD: radial diffusivity (mm^2/s); AD: axial diffusivity (mm^2/s); KA: kurtosis anisotropy; MK: mean kurtosis; RK: radial kurtosis; AK: axial kurtosis; MWF: myelin water fraction; IEWF: intra- and extracellular water fraction; IEW-gmT2: geometric mean T2 time of intra-and extracellular water (s); G-gmT2: geometric mean T2 time of general T2 distribution (s); NDI: neurite density index; ODI: orientation dispersion index; FISO: isotropic fraction

Figure 3.

Linear correlation coefficients of metrics with age. Cell values in black represent correlation coefficients that are significant ($p<0.05$) at uncorrected level. Cell values in white represent correlation coefficients that are significant ($p_{FWE}<0.05$) after controlling the family-wise error. The order of ROIs and metrics depends on the mean R^2 of linear (standard) or quadratic fit (if significantly better): ROIs are ranked in order of decreasing mean R^2 across metrics and metrics are ranked in descending order of mean R^2 across ROIs. The color labels correspond to the JHU ROIs used for analysis, as illustrated on the axial brain slices (below).

Figure 4.

Quadratic correlation coefficients of metrics with age. A positive sign indicates U-shaped curve and a negative sign indicates an inverse U-shaped curve. Cell values in black represent correlation coefficients that are significant ($p<0.05$) at uncorrected level. Cell values in white represent correlation coefficients that are significant ($p_{FWE}<0.05$) after controlling the family-wise error. Cells with a black border indicate the quadratic fit is significantly better than the linear fit from

Figure 3. For comparison, ROIs and metrics are ranked in the same way as in Figure 3. The color labels correspond to the JHU ROIs used for analysis, as illustrated on the axial brain slices (below).

Figure 5.

Scatter plots illustrating ROIs where quadratic fit with age is significantly better than a linear fit (red = female, blue = male). Panel A: intra- and extracellular water fraction in the fornix stria terminalis increases again with age after a minimum is reached between 40 and 50 years of age. Panel B: Orientation dispersion of neurites in the retrolenticular part of the internal capsule. Panel C: Radial diffusivity in the sagittal stratum. D: Mean kurtosis in the anterior limbs of the internal capsule

Figure 6.

Statistical parametric maps from voxel-based linear regression of WM diffusion tensor parameters with age. FA: fractional anisotropy, MD: mean diffusivity, RD: radial diffusivity, AD: axial diffusivity. The blue color scale indicates negative correlation ($r<0$) with age. The red scale indicates positive correlation ($r>0$) with age. DTI metrics reveal increasing isotropic diffusion with the most significant differences in frontal WM.

Figure 7.

Statistical parametric maps from voxel-based linear regression of WM kurtosis parameters with age. KA: kurtosis anisotropy, MK: mean kurtosis, RK: radial kurtosis, AK: axial kurtosis. The blue color scale indicates negative correlation with age. The red scale indicates positive correlation with age. DKI metrics showed minor but widespread differences with age. The most significant differences were found in regions near the corona radiata.

Figure 8.

Statistical parametric maps from voxel-based linear regression of WM NODDI parameters with age. FISO: isotropic fraction, NDI: neurite density index, ODI:

orientation dispersion index. The red scale indicates positive correlation with age. NODDI metrics reveal a large and widespread increase in isotropic diffusion. NDI expressed increased neurite density mainly in superior parietal WM (corona radiata). Differences in ODI were located in frontal WM, superior parietal WM and regions of crossing white matter pathways.

Figure 9.

Statistical parametric maps from voxel-based linear regression of WM MET2 parameters with age. MWF: myelin water fraction, IEWF: intra-and extracellular water fraction, IEW-gmT2: geometric mean T2 time of intra- and extracellular water, G-gmT2: geometric mean T2 time of general T2 distribution. The blue color scale indicates negative correlation with age. The red scale indicates positive correlation with age. MWF did not change significantly in frontal WM but in parallel with IEWF showed largest differences in the midbrain. IEW-gmT2 and to a less extent G-gmT2 showed frontal and superior parietal increases with age.

Figure 10.

The shared variance of metric values averaged over the cerebral WM mask expressed as a percentage (The higher the shared variance between two metrics, the better differences in one metric explain differences in the other metric). Red and blue color scales additionally indicate whether two metrics are positively ($r>0$) or negatively ($r<0$) correlated, respectively. Non-significant values, controlling the family-wise error at $p=0.05$ level, are displayed in grey. Kurtosis metrics (AK, MK, RK, KA) and NDI correlated well with MWF and IEWF. Mean kurtosis correlated well with neurite density index

Table 1

Summary of metrics used in this study. Adapted from (Billiet, et al., 2014a). Panel A) Summary of dMRI techniques, models and derived parameters used in the present study. FA = fractional anisotropy, MD = mean diffusivity, RD = radial diffusivity, AD = axial diffusivity, MK = mean kurtosis, RK = radial kurtosis, AK = axial kurtosis, KA = kurtosis anisotropy, FISO = isotropic fraction, NDI = neurite

density index, ODI = orientation dispersion index. Panel B) Summary of myelin water imaging model and derived parameters used in the present study. MWF = myelin water fraction, IEWF = intra- and extracellular water fraction, IEW-gmT2 = geometric mean T2 time of intra- and extracellular water, G-gmT2 = geometric mean T2 time of general T2 distribution

Supplementary Table 1:
Mean size and standard deviation of total cerebral WM and regions of interest from John Hopkins University white matter atlas (Mori, et al., 2005) after applying WM masks as described in section 2.3.3.

Supplementary Figure 1
Percentage of overlap of each individual's white matter mask. Values represent the frequency that a voxel of the WM mask as described in section 2.3.3 was classified as white matter across participants (i.e. individual segmentation higher than 0.8)

Supplementary Figure 2
Comparison of 'youngest' and 'oldest' white matter masks. Red = mean white matter segmentation of six youngest participants (age = 19.2 ± 1; 3 males) thresholded at 0.8. Green = mean white matter segmentation of six oldest participants (age = 62.3 ±24; 3 males). Blue = overlap between white matter masks of both subgroups. A large overlap is seen throughout the white matter illustrating little age-related differences due to registration.

References

Ashburner, J. 2007. A fast diffeomorphic image registration algorithm. Neuroimage 38(1), 95-113. doi:10.1016/j.neuroimage.2007.07.007.

Avants, B.B., Epstein, C.L., Grossman, M., Gee, J.C. 2008. Symmetric diffeomorphic image registration with cross-correlation: evaluating automated labeling of elderly and neurodegenerative brain. Med Image Anal 12(1), 26-41. doi:10.1016/j.media.2007.06.004.

Bartzokis, G., Lu, P.H., Heydari, P., Couvrette, A., Lee, G.J., Kalashyan, G., Freeman, F., Grinstead, J.W., Villablanca, P., Finn, J.P., Mintz, J., Alger, J.R., Altshuler, L.L. 2012. Multimodal Magnetic Resonance Imaging Assessment of White Matter Aging Trajectories Over the Lifespan of Healthy Individuals. Biol Psychiatry. doi:10.1016/j.biopsych.2012.07.010.

Basser, P.J., Mattiello, J., LeBihan, D. 1994. Estimation of the effective self-diffusion tensor from the NMR spin echo. J Magn Reson B 103(3), 247-54.

Beaulieu, C. 2002. The basis of anisotropic water diffusion in the nervous system - a technical review. NMR Biomed 15(7-8), 435-55. doi:10.1002/nbm.782.

Beaulieu, C., Allen, P.S. 1994. Determinants of anisotropic water diffusion in nerves. Magnetic resonance in medicine : official journal of the Society of Magnetic Resonance in Medicine / Society of Magnetic Resonance in Medicine 31(4), 394-400.

Billiet, T., Madler, B., D'Arco, F., Peeters, R., Deprez, S., Plasschaert, E., Leemans, A., Zhang, H., den Bergh, B.V., Vandenbulcke, M., Legius, E., Sunaert, S., Emsell, L. 2014a. Characterizing the microstructural basis of "unidentified bright objects" in neurofibromatosis type 1: A combined in vivo multicomponent T2 relaxation and multi-shell diffusion MRI analysis. Neuroimage Clin 4, 649-58. doi:10.1016/j.nicl.2014.04.005.

Billiet, T., Madler, B., D'Arco, F., Peeters, R., Deprez, S., Plasschaert, E., Leemans, A., Zhang, H., den Bergh, B.V., Vandenbulcke, M., Legius, E., Sunaert, S., Emsell, L. 2014b. Characterizing the microstructural basis of "unidentified bright objects" in neurofibromatosis type 1: A combined in vivo multicomponent T2 relaxation and multi-shell diffusion MRI analysis. Neuroimage Clin 4, 649-58. doi:10.1016/j.nicl.2014.04.005.

Brickman, A.M., Meier, I.B., Korgaonkar, M.S., Provenzano, F.A., Grieve, S.M., Siedlecki, K.L., Wasserman, B.T., Williams, L.M., Zimmerman, M.E. 2012. Testing the white matter retrogenesis hypothesis of cognitive aging. Neurobiol Aging 33(8), 1699-715. doi:10.1016/j.neurobiolaging.2011.06.001.

Callaghan, M.F., Freund, P., Draganski, B., Anderson, E., Cappelletti, M., Chowdhury, R., Diedrichsen, J., Fitzgerald, T.H., Smittenaar, P., Helms, G., Lutti, A., Weiskopf, N. 2014. Widespread age-related differences in the human brain microstructure revealed by quantitative magnetic resonance imaging. Neurobiol Aging 35(8), 1862-72. doi:10.1016/j.neurobiolaging.2014.02.008.

Coutu, J.P., Chen, J.J., Rosas, H.D., Salat, D.H. 2014. Non-Gaussian water diffusion in aging white matter. Neurobiol Aging 35(6), 1412-21. doi:10.1016/j.neurobiolaging.2013.12.001.

Davis, S.W., Dennis, N.A., Buchler, N.G., White, L.E., Madden, D.J., Cabeza, R. 2009. Assessing the effects of age on long white matter tracts using diffusion tensor tractography. Neuroimage 46(2), 530-41.

De Santis, S., Drakesmith, M., Bells, S., Assaf, Y., Jones, D.K. 2014. Why diffusion tensor MRI does well only some of the time: variance and covariance of white matter tissue microstructure attributes in the living human brain. Neuroimage 89, 35-44. doi:10.1016/j.neuroimage.2013.12.003.

Deoni, S.C., Dean, D.C., 3rd, O'Muircheartaigh, J., Dirks, H., Jerskey, B.A. 2012. Investigating white matter development in infancy and early childhood using myelin water faction and relaxation time mapping. Neuroimage 63(3), 1038-53. doi:10.1016/j.neuroimage.2012.07.037.

Draganski, B., Ashburner, J., Hutton, C., Kherif, F., Frackowiak, R.S., Helms, G., Weiskopf, N. 2011. Regional specificity of MRI contrast parameter changes in normal ageing revealed by voxel-based quantification (VBQ). Neuroimage 55(4), 1423-34. doi:10.1016/j.neuroimage.2011.01.052.

Falangola, M.F., Jensen, J.H., Babb, J.S., Hu, C., Castellanos, F.X., Di Martino, A., Ferris, S.H., Helpern, J.A. 2008. Age-related non-Gaussian diffusion patterns in the prefrontal brain. J Magn Reson Imaging 28(6), 1345-50. doi:10.1002/jmri.21604.

Fjell, A.M., Westlye, L.T., Amlien, I., Espeseth, T., Reinvang, I., Raz, N., Agartz, I., Salat, D.H., Greve, D.N., Fischl, B., Dale, A.M., Walhovd, K.B. 2009. High consistency of regional cortical thinning in aging across multiple samples. Cereb Cortex 19(9), 2001-12. doi:10.1093/cercor/bhn232.

Flynn, S.W., Lang, D.J., Mackay, A.L., Goghari, V., Vavasour, I.M., Whittall, K.P., Smith, G.N., Arango, V., Mann, J.J., Dwork, A.J., Falkai, P., Honer, W.G. 2003. Abnormalities of myelination in schizophrenia detected in vivo with MRI, and post-mortem with analysis of oligodendrocyte proteins. Mol Psychiatry 8(9), 811-20. doi:10.1038/sj.mp.4001337.

Frazier, J.A., Chiu, S., Breeze, J.L., Makris, N., Lange, N., Kennedy, D.N., Herbert, M.R., Bent, E.K., Koneru, V.K., Dieterich, M.E., Hodge, S.M., Rauch, S.L., Grant, P.E., Cohen, B.M., Seidman, L.J., Caviness, V.S., Biederman, J. 2005. Structural brain magnetic resonance imaging of limbic and thalamic volumes in pediatric bipolar disorder. The American journal of psychiatry 162(7), 1256-65. doi:10.1176/appi.ajp.162.7.1256.

Gong, N.J., Wong, C.S., Chan, C.C., Leung, L.M., Chu, Y.C. 2014. Aging in deep gray matter and white matter revealed by diffusional kurtosis imaging. Neurobiol Aging 35(10), 2203-16. doi:10.1016/j.neurobiolaging.2014.03.011.

Haroutunian, V., Katsel, P., Roussos, P., Davis, K.L., Altshuler, L.L., Bartzokis, G. 2014. Myelination, oligodendrocytes, and serious mental illness. Glia. doi:10.1002/glia.22716.

Hennig, J. 1988. Multiecho Imaging Sequences with Low Refocusing Flip Angles. J Magn Reson 78(3), 397-407. doi:Doi 10.1016/0022-2364(88)90128-X.

Hui, E.S., Cheung, M.M., Qi, L., Wu, E.X. 2008. Towards better MR characterization of neural tissues using directional diffusion kurtosis analysis. Neuroimage 42(1), 122-34. doi:10.1016/j.neuroimage.2008.04.237.

Inano, S., Takao, H., Hayashi, N., Abe, O., Ohtomo, K. 2011. Effects of age and gender on white matter integrity. AJNR Am J Neuroradiol 32(11), 2103-9. doi:10.3174/ajnr.A2785.

Irfanoglu, M.O., Walker, L., Sarlls, J., Marenco, S., Pierpaoli, C. 2012. Effects of image distortions originating from susceptibility variations and concomitant fields on diffusion MRI tractography results. Neuroimage 61(1), 275-88. doi:10.1016/j.neuroimage.2012.02.054.

Jelescu, I.O., Veraart, J., Adisetiyo, V., Milla, S.S., Novikov, D.S., Fieremans, E. 2015. One diffusion acquisition and different white matter models: How does microstructure change in human early development based on WMTI and NODDI? Neuroimage 107, 242-56. doi:10.1016/j.neuroimage.2014.12.009.

Jensen, J.H., Helpern, J.A. 2010. MRI quantification of non-Gaussian water diffusion by kurtosis analysis. NMR Biomed 23(7), 698-710. doi:10.1002/nbm.1518.

Jensen, J.H., Helpern, J.A., Ramani, A., Lu, H., Kaczynski, K. 2005. Diffusional kurtosis imaging: the quantification of non-gaussian water diffusion by means of magnetic resonance imaging. Magnetic resonance in medicine : official journal of the Society of Magnetic Resonance in Medicine / Society of Magnetic Resonance in Medicine 53(6), 1432-40. doi:10.1002/mrm.20508.

Jones, D.K., Cercignani, M. 2010. Twenty-five pitfalls in the analysis of diffusion MRI data. NMR Biomed 23(7), 803-20. doi:10.1002/nbm.1543.

Kempton, M.J., Underwood, T.S., Brunton, S., Stylios, F., Schmechtig, A., Ettinger, U., Smith, M.S., Lovestone, S., Crum, W.R., Frangou, S., Williams, S.C., Simmons, A. 2011. A comprehensive testing protocol for MRI neuroanatomical segmentation techniques: Evaluation of a novel lateral ventricle segmentation method. Neuroimage 58(4), 1051-9. doi:10.1016/j.neuroimage.2011.06.080.

Kumar, R., Chavez, A.S., Macey, P.M., Woo, M.A., Harper, R.M. 2013. Brain axial and radial diffusivity changes with age and gender in healthy adults. Brain Res 1512, 22-36. doi:10.1016/j.brainres.2013.03.028.

Kunz, N., Zhang, H., Vasung, L., O'Brien, K.R., Assaf, Y., Lazeyras, F., Alexander, D.C., Huppi, P.S. 2014. Assessing white matter microstructure of the newborn with multi-shell diffusion MRI and biophysical compartment models. Neuroimage 96, 288-99. doi:10.1016/j.neuroimage.2014.03.057.

Lally, P., Zhang, H., Pauliah, S., Price, D., Bainbridge, A., Balraj, G., Cady, E., Shankaran, S., Thayyil, S. 2014. 8.9 Microstructural Changes in Neonatal Encephalopathy Revealed with the Neurite Orientation Dispersion and Density Imaging (NODDI) Model. Arch Dis Child Fetal Neonatal Ed 99 Suppl 1, A14. doi:10.1136/archdischild-2014-306576.38.

Latt, J., Nilsson, M., Wirestam, R., Stahlberg, F., Karlsson, N., Johansson, M., Sundgren, P.C., van Westen, D. 2013. Regional values of diffusional kurtosis estimates in the healthy brain. J Magn Reson Imaging 37(3), 610-8. doi:10.1002/jmri.23857.

Laule, C., Vavasour, I.M., Kolind, S.H., Traboulsee, A.L., Moore, G.R., Li, D.K., Mackay, A.L. 2007a. Long T2 water in multiple sclerosis: what else can we learn from multi-echo T2 relaxation? J Neurol 254(11), 1579-87. doi:10.1007/s00415-007-0595-7.

Laule, C., Vavasour, I.M., Madler, B., Kolind, S.H., Sirrs, S.M., Brief, E.E., Traboulsee, A.L., Moore, G.R., Li, D.K., MacKay, A.L. 2007b. MR evidence of long T2 water in pathological white matter. J Magn Reson Imaging 26(4), 1117-21. doi:10.1002/jmri.21132.

Lebel, C., Gee, M., Camicioli, R., Wieler, M., Martin, W., Beaulieu, C. 2012. Diffusion tensor imaging of white matter tract evolution over the lifespan. Neuroimage 60(1), 340-52. doi:10.1016/j.neuroimage.2011.11.094.

Leemans, A. 2009. ExploreDTI: a graphical toolbox for processing, analyzing, and visualizing diffusion MR data. 17th Annual Meeting of Intl Soc Mag Reson Med, Hawaii, USA, pp p. 3537.

Leemans, A., Jones, D.K. 2009. The B-Matrix Must Be Rotated When Correcting for Subject Motion in DTI Data. Magnet Reson Med 61(6), 1336-49. doi:Doi 10.1002/Mrm.21890.

Madden, D.J., Whiting, W.L., Huettel, S.A., White, L.E., MacFall, J.R., Provenzale, J.M. 2004. Diffusion tensor imaging of adult age differences in cerebral white matter: relation to response time. Neuroimage 21(3), 1174-81. doi:10.1016/j.neuroimage.2003.11.004.

Madler, B., Drabycz, S.A., Kolind, S.H., Whittall, K.P., MacKay, A.L. 2008. Is diffusion anisotropy an accurate monitor of myelination? Correlation of multicomponent T2 relaxation and diffusion tensor anisotropy in human brain. Magn Reson Imaging 26(7), 874-88. doi:10.1016/j.mri.2008.01.047.

Maedler, B., MacKay, A. 2007. Towards whole brain myelin imaging. International Society for Magnetic Resonance in Medicine, Berlin, Germany, pp 1723.

Melbourne, A., Eaton-Rosen, Z., Bainbridge, A., Kendall, G.S., Cardoso, M.J., Robertson, N.J., Marlow, N., Ourselin, S. 2013. Measurement of myelin in the preterm brain: multi-compartment diffusion

imaging and multi-component T2 relaxometry. Medical image computing and computer-assisted intervention : MICCAI International Conference on Medical Image Computing and Computer-Assisted Intervention 16(Pt 2), 336-44.

Mori, S., Wakana, S., Nagae-Poetscher, L.M., P.C.M., v.Z. 2005. MRI Atlas of Human White Matter. Elsevier.

Pannese, E. 2011. Morphological changes in nerve cells during normal aging. Brain Struct Funct 216(2), 85-9. doi:10.1007/s00429-011-0308-y.

Pfefferbaum, A., Sullivan, E.V., Hedehus, M., Lim, K.O., Adalsteinsson, E., Moseley, M. 2000. Age-related decline in brain white matter anisotropy measured with spatially corrected echo-planar diffusion tensor imaging. Magnetic resonance in medicine : official journal of the Society of Magnetic Resonance in Medicine / Society of Magnetic Resonance in Medicine 44(2), 259-68.

Poot, D.H., den Dekker, A.J., Achten, E., Verhoye, M., Sijbers, J. 2010. Optimal experimental design for diffusion kurtosis imaging. IEEE Trans Med Imaging 29(3), 819-29. doi:10.1109/TMI.2009.2037915.

Prasloski, T., Madler, B., Xiang, Q.S., Mackay, A., Jones, C. 2011. Applications of stimulated echo correction to multicomponent T(2) analysis. Magnetic resonance in medicine : official journal of the Society of Magnetic Resonance in Medicine / Society of Magnetic Resonance in Medicine. doi:10.1002/mrm.23157.

Prasloski, T., Rauscher, A., MacKay, A.L., Hodgson, M., Vavasour, I.M., Laule, C., Madler, B. 2012. Rapid whole cerebrum myelin water imaging using a 3D GRASE sequence. Neuroimage 63(1), 533-9. doi:10.1016/j.neuroimage.2012.06.064.

Raz, N., Gunning, F.M., Head, D., Dupuis, J.H., McQuain, J., Briggs, S.D., Loken, W.J., Thornton, A.E., Acker, J.D. 1997. Selective aging of the human cerebral cortex observed in vivo: differential vulnerability of the prefrontal gray matter. Cereb Cortex 7(3), 268-82.

Salat, D.H., Lee, S.Y., van der Kouwe, A.J., Greve, D.N., Fischl, B., Rosas, H.D. 2009. Age-associated alterations in cortical gray and white matter signal intensity and gray to white matter contrast. Neuroimage 48(1), 21-8. doi:10.1016/j.neuroimage.2009.06.074.

Salat, D.H., Tuch, D.S., Greve, D.N., van der Kouwe, A.J., Hevelone, N.D., Zaleta, A.K., Rosen, B.R., Fischl, B., Corkin, S., Rosas, H.D., Dale, A.M. 2005. Age-related alterations in white matter microstructure measured by diffusion tensor imaging. Neurobiol Aging 26(8), 1215-27. doi:10.1016/j.neurobiolaging.2004.09.017.

Song, S.K., Yoshino, J., Le, T.Q., Lin, S.J., Sun, S.W., Cross, A.H., Armstrong, R.C. 2005. Demyelination increases radial diffusivity in corpus callosum of mouse brain. Neuroimage 26(1), 132-40. doi:Doi 10.1016/J.Neuroimage.2005.01.028.

Stanisz, G.J., Webb, S., Munro, C.A., Pun, T., Midha, R. 2004. MR properties of excised neural tissue following experimentally induced inflammation. Magnetic resonance in medicine : official journal of the Society of Magnetic Resonance in Medicine / Society of Magnetic Resonance in Medicine 51(3), 473-9. doi:10.1002/mrm.20008.

Sullivan, E.V., Pfefferbaum, A. 2006. Diffusion tensor imaging and aging. Neurosci Biobehav R 30(6), 749-61. doi:10.1016/j.neubiorev.2006.06.002.

Tournier, J.D., Mori, S., Leemans, A. 2011. Diffusion tensor imaging and beyond. Magn Reson Med 65(6), 1532-56. doi:10.1002/mrm.22924.

Van Hecke, W., Leemans, A., D'Agostino, E., De Backer, S., Vandervliet, E., Parizel, P.M., Sijbers, J. 2007. Nonrigid coregistration of diffusion tensor images using a viscous fluid model and mutual information. IEEE Trans Med Imaging 26(11), 1598-612. doi:Doi 10.1109/Tmi.2007.906786.

Van Hecke, W., Leemans, A., Sage, C.A., Emsell, L., Veraart, J., Sijbers, J., Sunaert, S., Parizel, P.M. 2011. The effect of template selection on diffusion tensor voxel-based analysis results. Neuroimage 55(2), 566-73. doi:10.1016/j.neuroimage.2010.12.005.

Vavasour, I.M., Laule, C., Li, D.K., Traboulsee, A.L., MacKay, A.L. 2011. Is the magnetization transfer ratio a marker for myelin in multiple sclerosis? J Magn Reson Imaging 33(3), 713-8. doi:10.1002/jmri.22441.

Vos, S.B., Jones, D.K., Viergever, M.A., Leemans, A. 2011. Partial volume effect as a hidden covariate in DTI analyses. Neuroimage 55(4), 1566-76. doi:Doi 10.1016/J.Neuroimage.2011.01.048.

Wheeler-Kingshott, C.A., Cercignani, M. 2009. About "axial" and "radial" diffusivities. Magnetic resonance in medicine : official journal of the Society of Magnetic Resonance in Medicine / Society of Magnetic Resonance in Medicine 61(5), 1255-60. doi:10.1002/mrm.21965.

Whitaker, K.J., Kolind, S.H., MacKay, A.L., Clark, C.M. 2008. Quantifying development: Investigating highly myelinated voxels in preadolescent corpus callosum. Neuroimage 43(4), 731-5. doi:10.1016/j.neuroimage.2008.07.038.

Whittall, K.P., Mackay, A.L. 1989. Quantitative Interpretation of Nmr Relaxation Data. J Magn Reson 84(1), 134-52. doi:Doi 10.1016/0022-2364(89)90011-5.

Winston, G.P., Micallef, C., Symms, M.R., Alexander, D.C., Duncan, J.S., Zhang, H. 2014. Advanced diffusion imaging sequences could aid assessing patients with focal cortical dysplasia and epilepsy. Epilepsy Res 108(2), 336-9. doi:10.1016/j.eplepsyres.2013.11.004.

Zhang, H., Schneider, T., Wheeler-Kingshott, C.A., Alexander, D.C. 2012. NODDI: practical in vivo neurite orientation dispersion and density imaging of the human brain. Neuroimage 61(4), 1000-16. doi:10.1016/j.neuroimage.2012.03.072.

A) Diffusion MRI (dMRI)

Model	Measure	Measure relates to	Influenced by which microstructural feature(s)	Scale
DTI	FA	Presence of preferred direction of diffusion (i.e. anisotropy)	Axonal organisation, presence of coherently organised structures / membranes	0 – 1 (0 = most isotropic, 1 = most anisotropic)
	MD	Amount of isotropic diffusion	Relative presence of CSF and extracellular water (i.e. water not bounded by membranes, e.g. in CSF or extracellular tissue)	Continuous (Increasing value = increasing amount of diffusion)
	RD	Amount of diffusion perpendicular to direction of largest diffusion	Relative presence of CSF and extracellular water along radial direction of diffusion. May relate to myelin content in isolated fiber populations.	Continuous (Increasing value = increasing amount of diffusion)
	AD	Amount of diffusion parallel to direction of largest diffusion	Relative presence of CSF and extracellular water along axial direction of diffusion. May relate to axon alignment in isolated fiber populations.	Continuous (Increasing value = increasing amount of diffusion)
DKI	MK	Deviation of mean diffusion displacement profile from a Gaussian curve	Sources of hindered and/or restricted diffusion, e.g. myelination, axon packing, membrane permeability	Continuous (Increasing value = more compartmentalization)
	RK	Extent to which the diffusion displacement profile perpendicular to the direction of largest diffusion deviates from a Gaussian curve	Sources of hindered and/or restricted diffusion perpendicular to axons	Continuous (Increasing value = more compartmentalization)
	AK	Extent to which the diffusion displacement profile parallel to the direction of largest diffusion deviates from a Gaussian curve	Sources of hindered and/or restricted diffusion parallel to axons	Continuous (Increasing value = more compartmentalization)
	KA	Presence of preferred direction in which non-Gaussian diffusion occurs	Dependency of hindered and/or restricted diffusion on the direction of diffusion	0 – 1 (0 = most isotropic compartmentalization, 1 = most anisotropic compartmentalization)

NODDI	FISO	Diffusion signal fraction with isotropic Gaussian properties	Cerebrospinal fluid fraction	0 – 1 (0 = no CSF-like fluid, 1 = most CSF-like fluid)
	NDI	Fraction of 1-FISO expressing unhindered diffusion along and restricted diffusion perpendicular to a set of sticks	Density of axons and dendrites based on intracellular diffusion	0 – 1 (0 = most extracellular diffusion, 1 = most intracellular diffusion)
	ODI	Tortuosity measure coupling an intracellular (set of sticks) and an extracellular space (diffusion tensor)	Dispersion of axons and dendrites in the intracellular compartment	0 – 1 (0 = well-aligned neurites, 1 = highly dispersed neurites)

B) Myelin Water Imaging (MWI)

Model	Measure	Measure relates to	Influenced by which microstructural feature(s)	Scale
MET2	MWF	Relative area fraction of signal having short T2 time (10-40ms) in a T2 distribution	Myelin content, absolute water content	0 – 1 (0 = least myelin, 1 = most myelin)
	IEWF	Relative area fraction of signal having intermediate T2 time (40-200ms) in a T2 distribution	Water molecules in and between axons (or having similar properties), absolute water content	0 – 1 (0 = no intra- or extracellular water, 1 = mostly intra- and extracellular water)
	IEW-gmT2	Position of IEW peak in the T2 distribution	Intra- and extra axonal mobility of water molecules (e.g. long T2 time = high mobility)	Continuous (Increasing value = more loosely bound water molecules)
	G-gmT2	Mean T2 time of general T2 distribution (i.e. conventional T2 time)	Mean mobility of water molecules (regardless of location)	Continuous (Increasing value = more loosely bound water molecules)

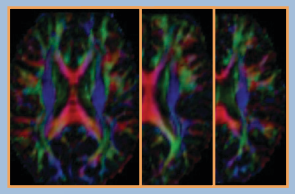

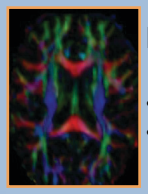

Representative subset of diffusion tensor maps (b=2800)

- Male: N = 15, age (mean/S.D./min./max.) = 41.2/14.0/19.3/64.3
- Female: N = 15, age (mean/S.D./min./max.) = 40.8/14.5/19.4/64.3

Creation of population-based template

Population-based template in register with MNI space

Aff. NR Tensor-based

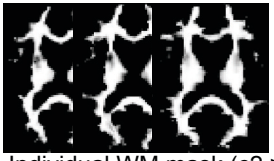

Individual WM mask (c2 > 0.8) (incl.)

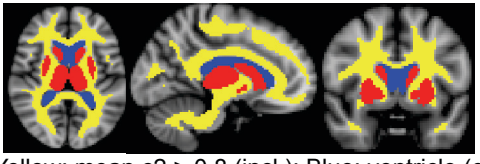

Yellow: mean c2 > 0.8 (incl.); Blue: ventricle (excl.); Red: basal ganglia and thalamus (excl.)

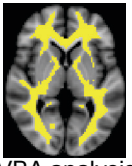

VBA analysis

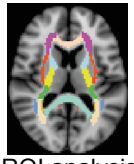

ROI analysis

dMRI space

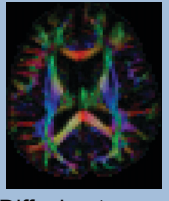

Diffusion tensor (b=2800)

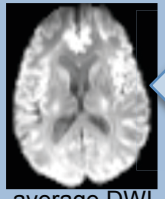

average DWI (b=1000)

FA (b=1000)

T1 space

Diff. MI

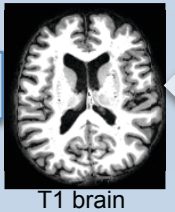

T1 brain

Diff. CC

T1 white matter

MET2 space

Affine MI

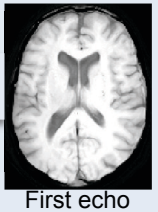

First echo

dMRI metrics: FA, MD, RD, AD, KA, MK, RL, AK, NDI, ODI, FISO

Tissue class images: c1 (GM), c2 (WM)

MET2 metrics: MWF, IEWF, IEW-gmT2, G-gmT2

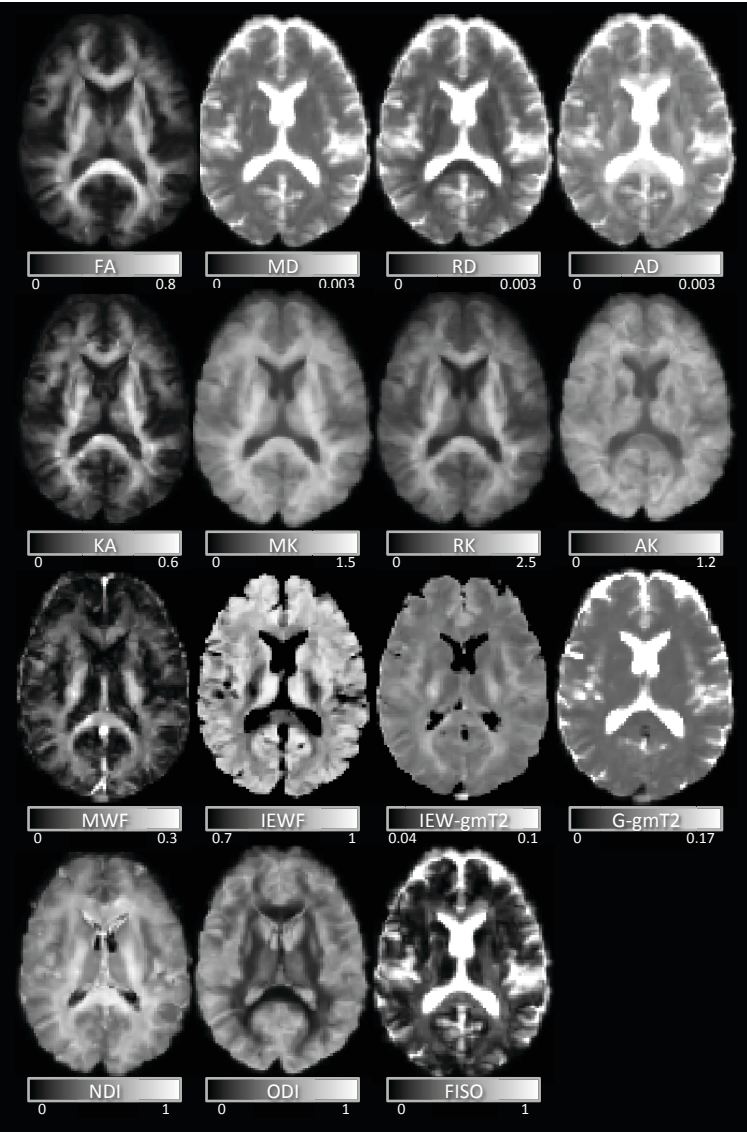
FA
0
0.8
MD
0
0.003
RD
0
0.003
AD
0
0.003
KA
0
0.6
MK
0
1.5
RK
0
2.5
AK
0
1.2
MWF
0
0.3
IEWF
0.7
1
IEW-gmT2
0.04
0.1
G-gmT2
0
0.17
NDI
0
1
ODI
0
1
FISO
0
1

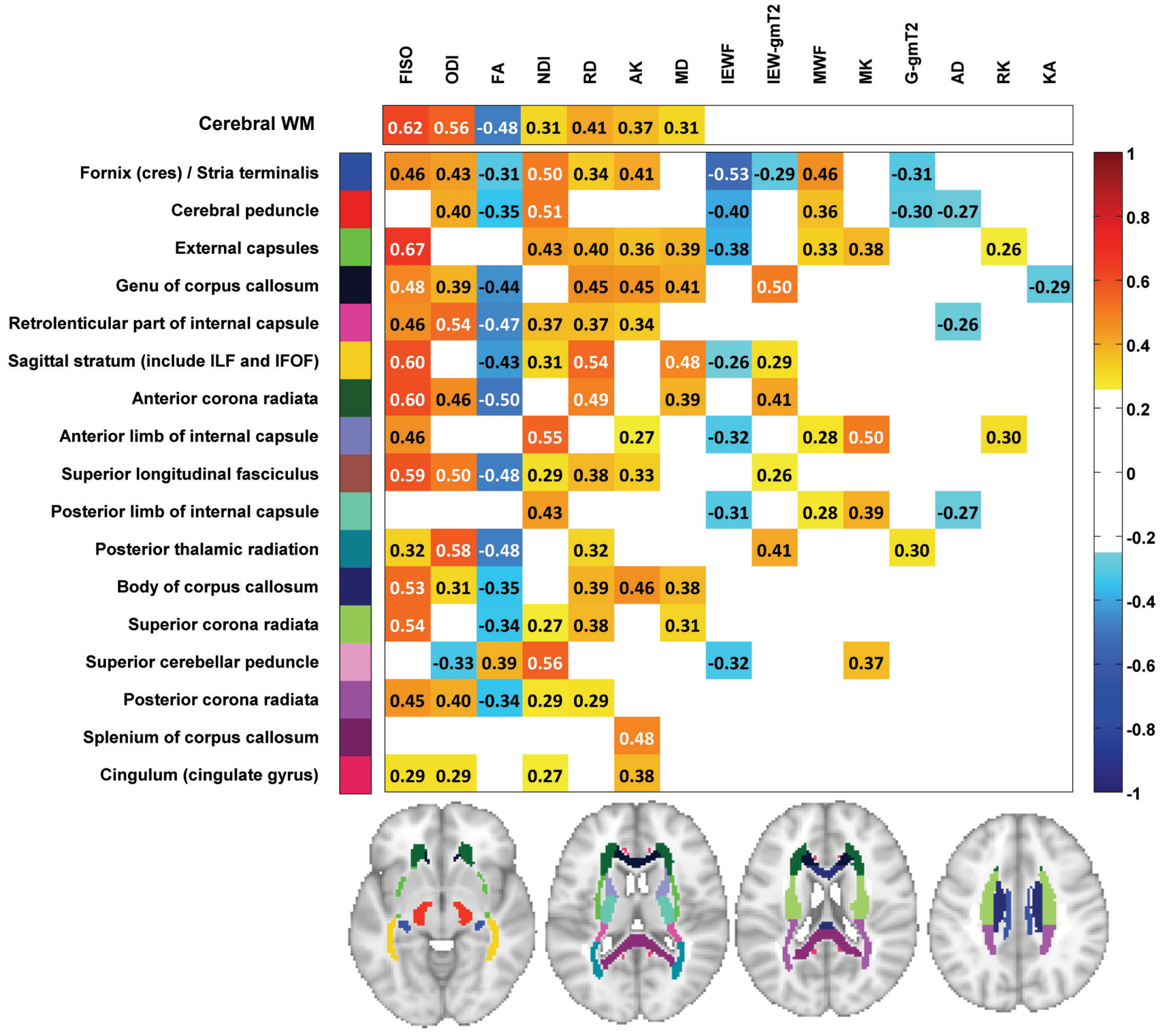
FISO
ODI
FA
NDI
RD
AK
MD
IEWF
IEW-gmT2
MWF
MK
G-gmT2
AD
RK
KA
Cerebral WM
0.62 0.56 -0.48 0.31 0.41 0.37 0.31
Fornix (cres) / Stria terminalis
0.46 0.43 -0.31 0.50 0.34 0.41 -0.53 -0.29 0.46 -0.31
Cerebral peduncle
0.40 -0.35 0.51 -0.40 0.36 -0.30 -0.27
External capsules
0.67 0.43 0.40 0.36 0.39 -0.38 0.33 0.38 0.26
Genu of corpus callosum
0.48 0.39 -0.44 0.45 0.45 0.41 0.50 -0.29
Retrolenticular part of internal capsule
0.46 0.54 -0.47 0.37 0.37 0.34 -0.26
Sagittal stratum (include ILF and IFOF)
0.60 -0.43 0.31 0.54 0.48 -0.26 0.29
Anterior corona radiata
0.60 0.46 -0.50 0.49 0.39 0.41
Anterior limb of internal capsule
0.46 0.55 0.27 -0.32 0.28 0.50 0.30
Superior longitudinal fasciculus
0.59 0.50 -0.48 0.29 0.38 0.33 0.26
Posterior limb of internal capsule
0.43 -0.31 0.28 0.39 -0.27
Posterior thalamic radiation
0.32 0.58 -0.48 0.32 0.41 0.30
Body of corpus callosum
0.53 0.31 -0.35 0.39 0.46 0.38
Superior corona radiata
0.54 -0.34 0.27 0.38 0.31
Superior cerebellar peduncle
-0.33 0.39 0.56 -0.32 0.37
Posterior corona radiata
0.45 0.40 -0.34 0.29 0.29
Splenium of corpus callosum
0.48
Cingulum (cingulate gyrus)
0.29 0.29 0.27 0.38
1
0.8
0.6
0.4
0.2
0
-0.2
-0.4
-0.6
-0.8
-1

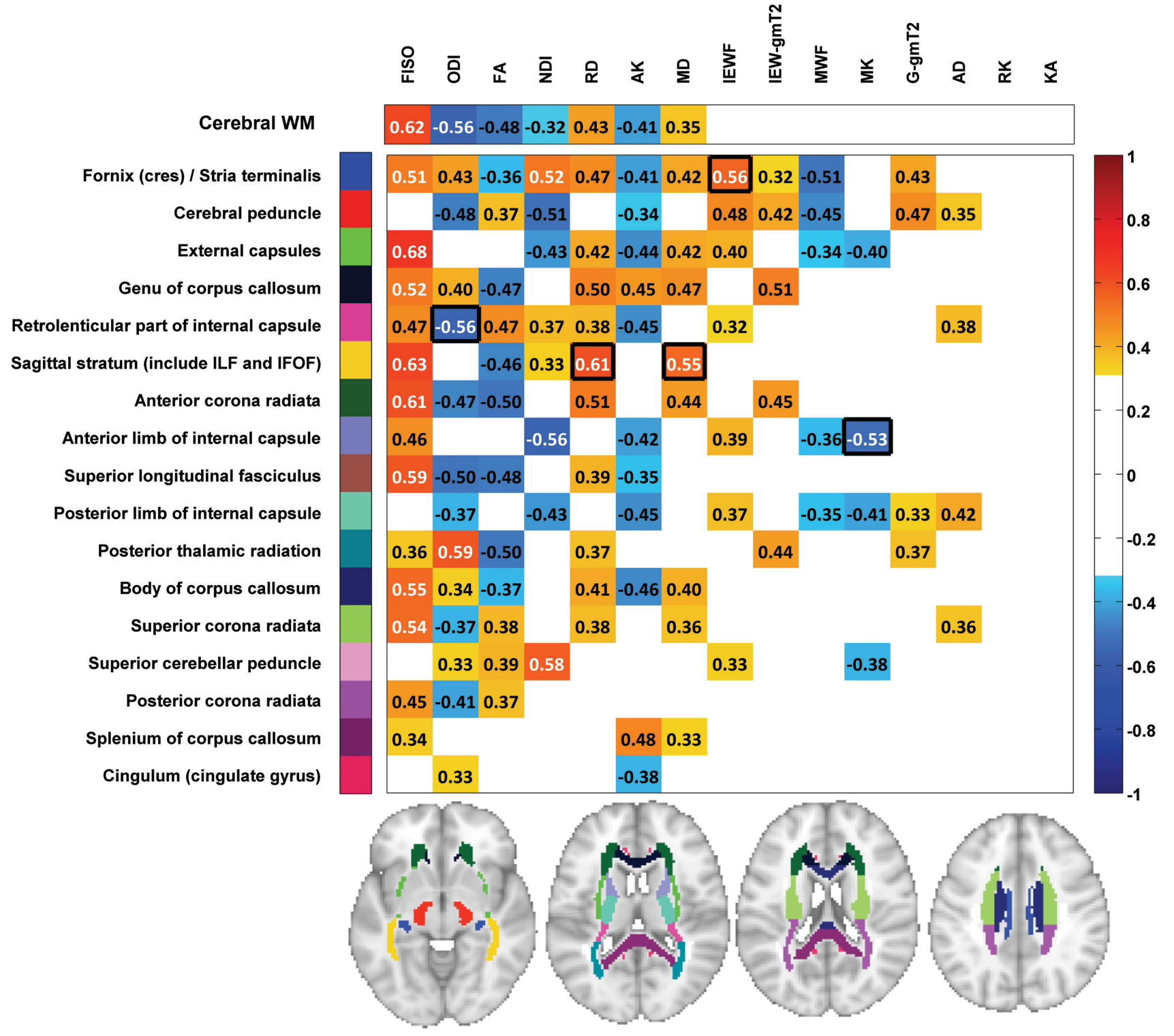
FISO
ODI
FA
NDI
RD
AK
MD
IEWF
IEW-gmT2
MWF
MK
G-gmT2
AD
RK
KA
Cerebral WM
0.62 -0.56 -0.48 -0.32 0.43 -0.41 0.35
Fornix (cres) / Stria terminalis
0.51 0.43 -0.36 0.52 0.47 -0.41 0.42 0.56 0.32 -0.51 0.43
Cerebral peduncle
-0.48 0.37 -0.51 -0.34 0.48 0.42 -0.45 0.47 0.35
External capsules
0.68 -0.43 0.42 -0.44 0.42 0.40 -0.34 -0.40
Genu of corpus callosum
0.52 0.40 -0.47 0.50 0.45 0.47 0.51
Retrolenticular part of internal capsule
0.47 -0.56 0.47 0.37 0.38 -0.45 0.32 0.38
Sagittal stratum (include ILF and IFOF)
0.63 -0.46 0.33 0.61 0.55
Anterior corona radiata
0.61 -0.47 -0.50 0.51 0.44 0.45
Anterior limb of internal capsule
0.46 -0.56 -0.42 0.39 -0.36 -0.53
Superior longitudinal fasciculus
0.59 -0.50 -0.48 0.39 -0.35
Posterior limb of internal capsule
-0.37 -0.43 -0.45 0.37 -0.35 -0.41 0.33 0.42
Posterior thalamic radiation
0.36 0.59 -0.50 0.37 0.44 0.37
Body of corpus callosum
0.55 0.34 -0.37 0.41 -0.46 0.40
Superior corona radiata
0.54 -0.37 0.38 0.38 0.36 0.36
Superior cerebellar peduncle
0.33 0.39 0.58 0.33 -0.38
Posterior corona radiata
0.45 -0.41 0.37
Splenium of corpus callosum
0.34 0.48 0.33
Cingulum (cingulate gyrus)
0.33 -0.38
1
0.8
0.6
0.4
0.2
0
-0.2
-0.4
-0.6
-0.8
-1

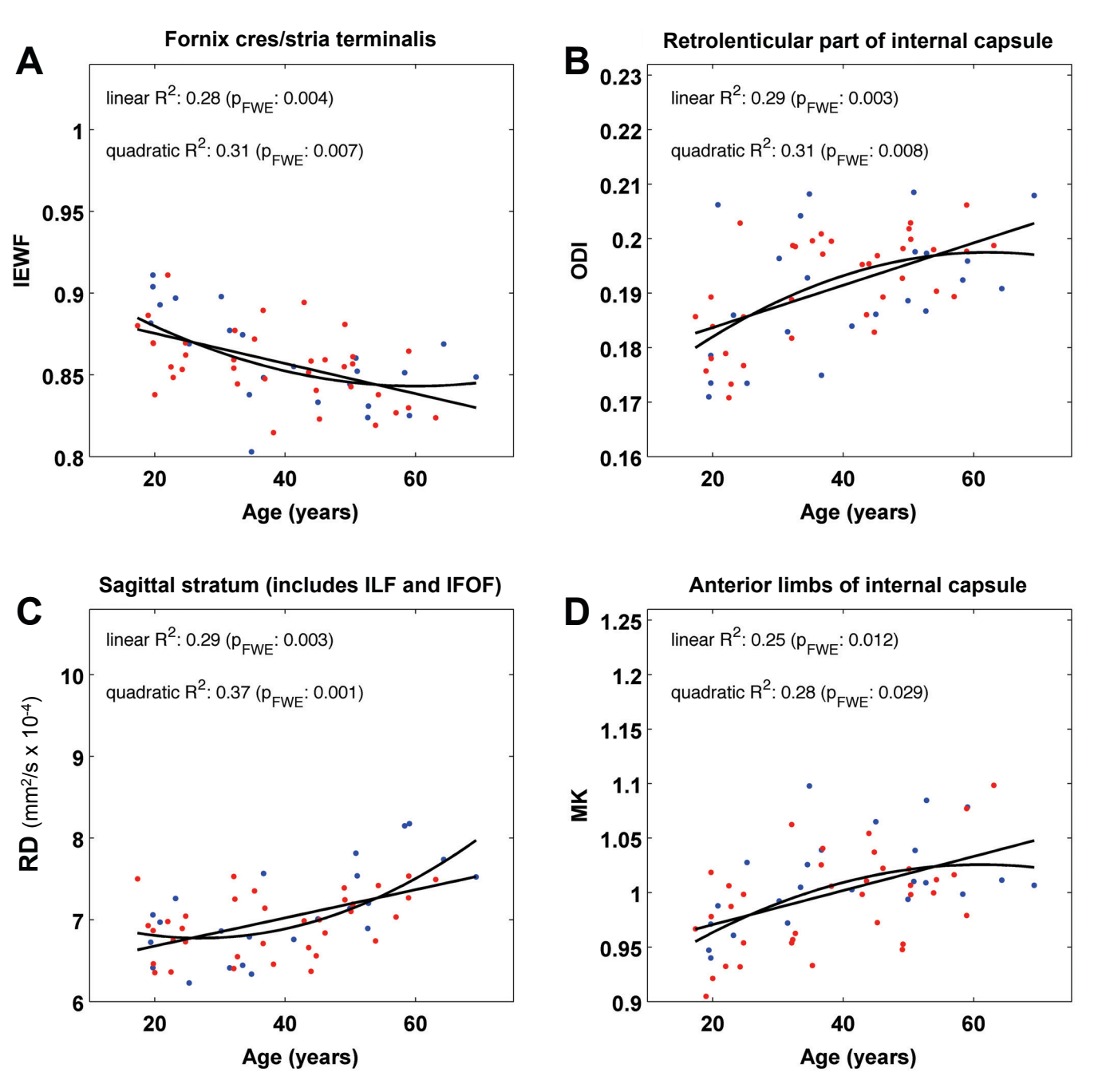
A
Fornix cres/stria terminalis
linear R2: 0.28 (pFWE: 0.004)
quadratic R2: 0.31 (pFWE: 0.007)
IEWF
Age (years)
B
Retrolenticular part of internal capsule
linear R2: 0.29 (pFWE: 0.003)
quadratic R2: 0.31 (pFWE: 0.008)
ODI
Age (years)
C
Sagittal stratum (includes ILF and IFOF)
linear R2: 0.29 (pFWE: 0.003)
quadratic R2: 0.37 (pFWE: 0.001)
RD (mm2/s x 10-4)
Age (years)
D
Anterior limbs of internal capsule
linear R2: 0.25 (pFWE: 0.012)
quadratic R2: 0.28 (pFWE: 0.029)
MK
Age (years)

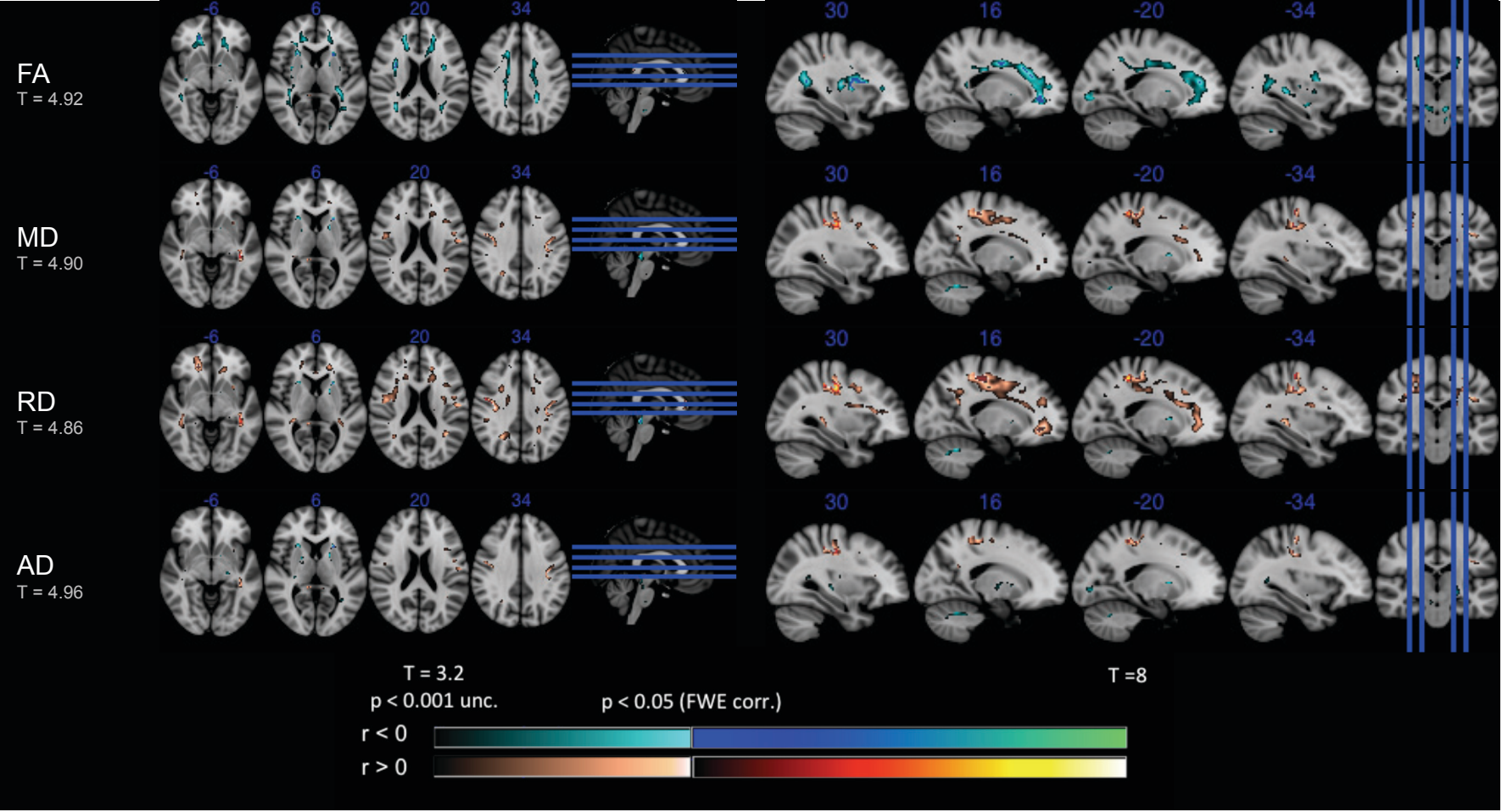
FA
T = 4.92
MD
T = 4.90
RD
T = 4.86
AD
T = 4.96
-6
6
20
34
30
16
-20
-34
T = 3.2
p < 0.001 unc.
p < 0.05 (FWE corr.)
T =8
r < 0
r > 0

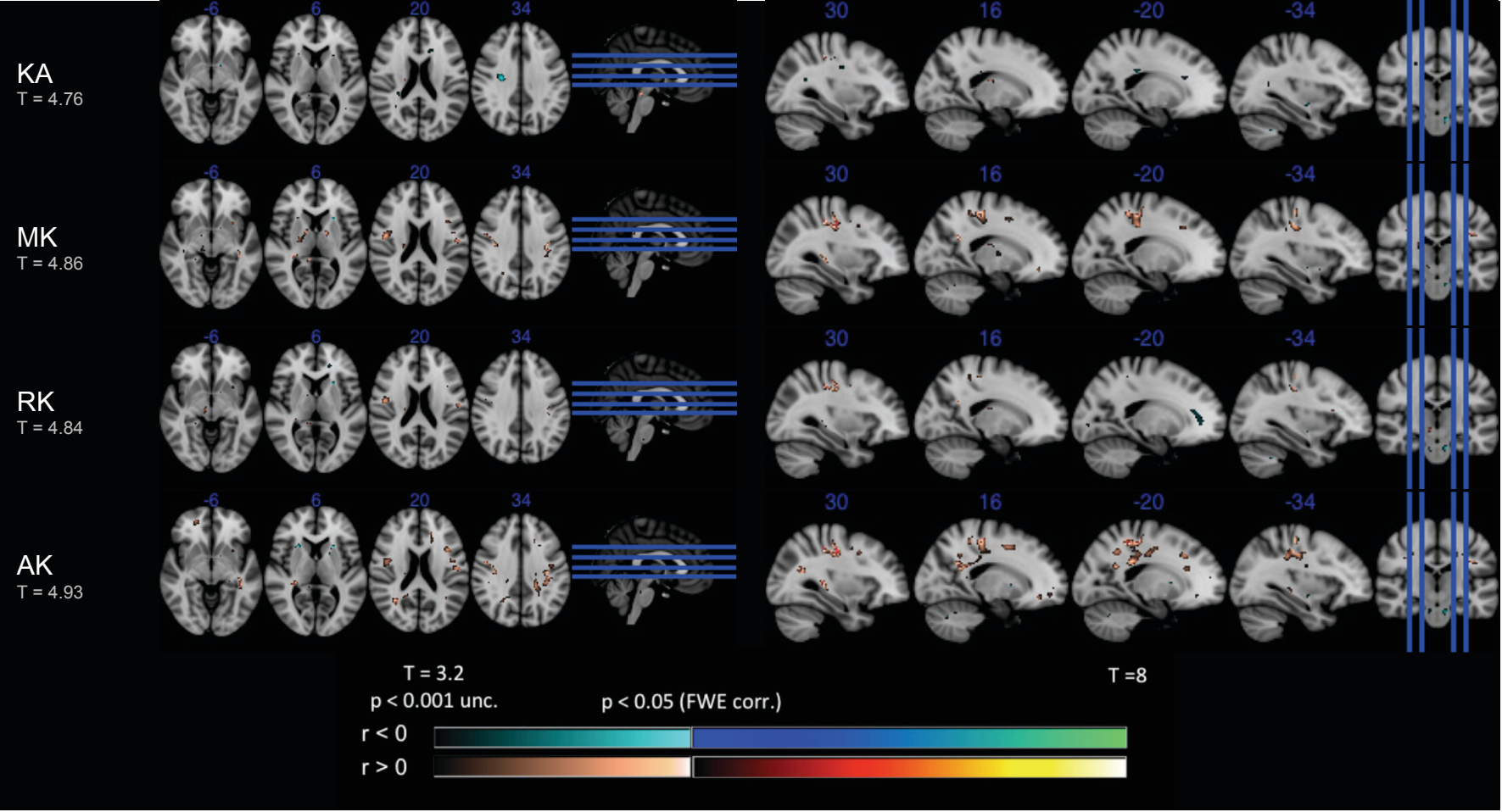
KA
T = 4.76
MK
T = 4.86
RK
T = 4.84
AK
T = 4.93
-6
6
20
34
30
16
-20
-34
T = 3.2
p < 0.001 unc.
p < 0.05 (FWE corr.)
T =8
r < 0
r > 0

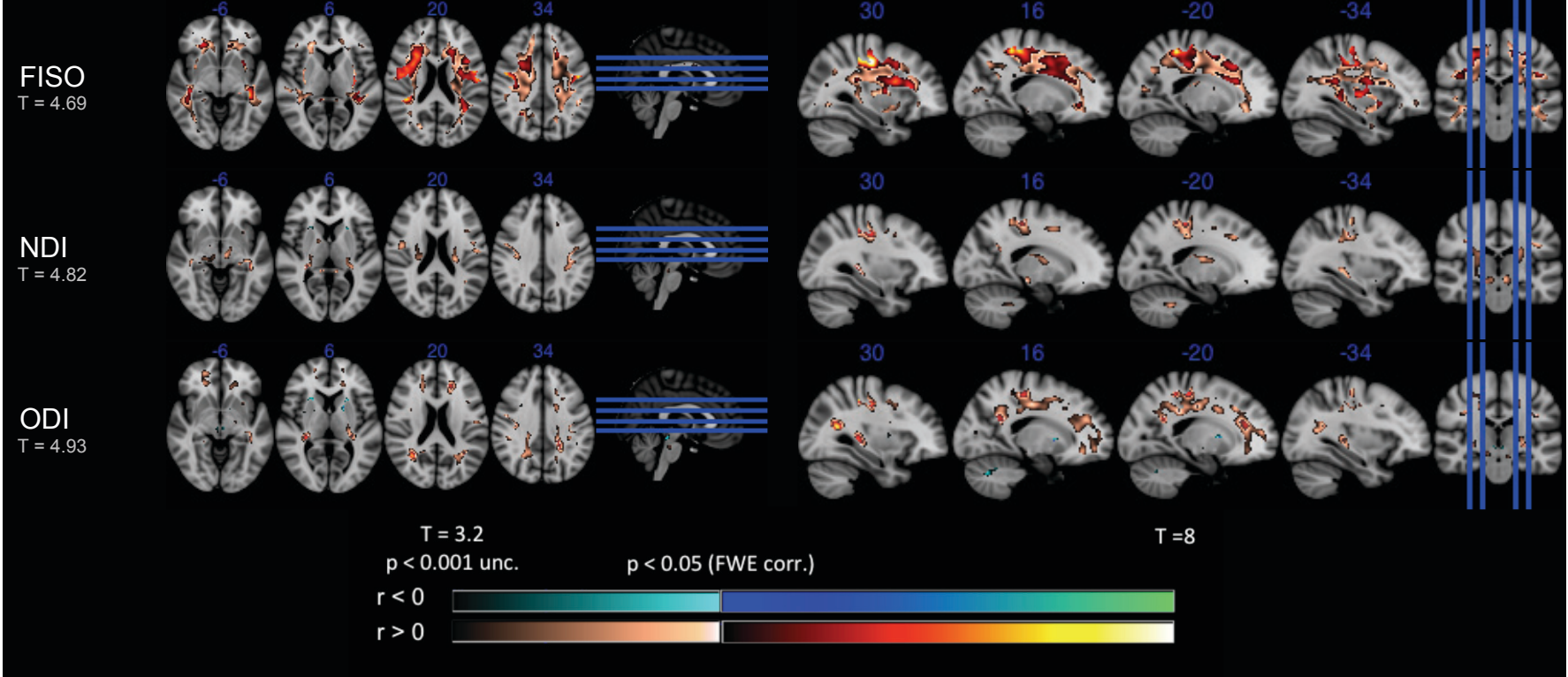
FISO
T = 4.69
NDI
T = 4.82
ODI
T = 4.93
-6
6
20
34
30
16
-20
-34
T = 3.2
p < 0.001 unc.
p < 0.05 (FWE corr.)
T =8
r < 0
r > 0

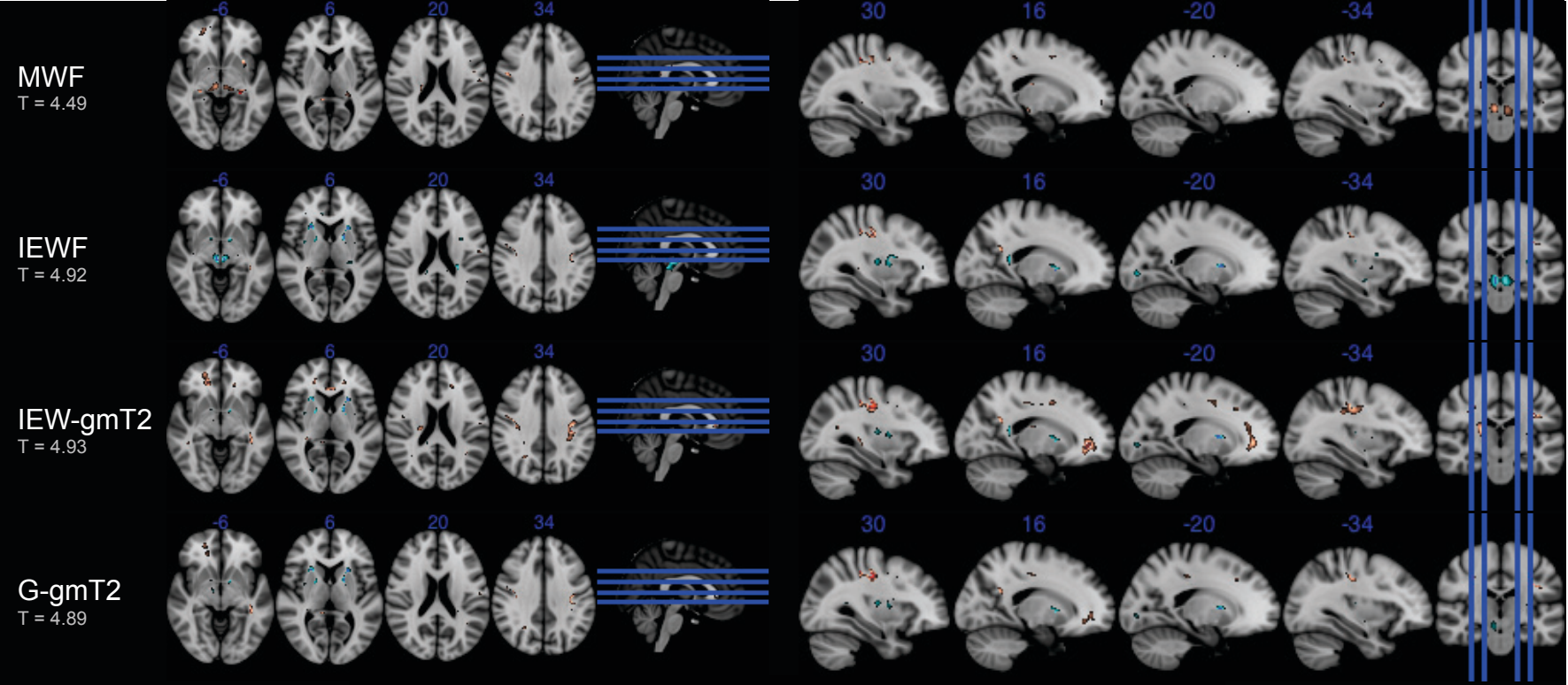
MWF
T = 4.49
IEWF
T = 4.92
IEW-gmT2
T = 4.93
G-gmT2
T = 4.89
-6
6
20
34
30
16
-20
-34
T = 3.2
p < 0.001 unc.
p < 0.05 (FWE corr.)
T =8
r < 0
r > 0

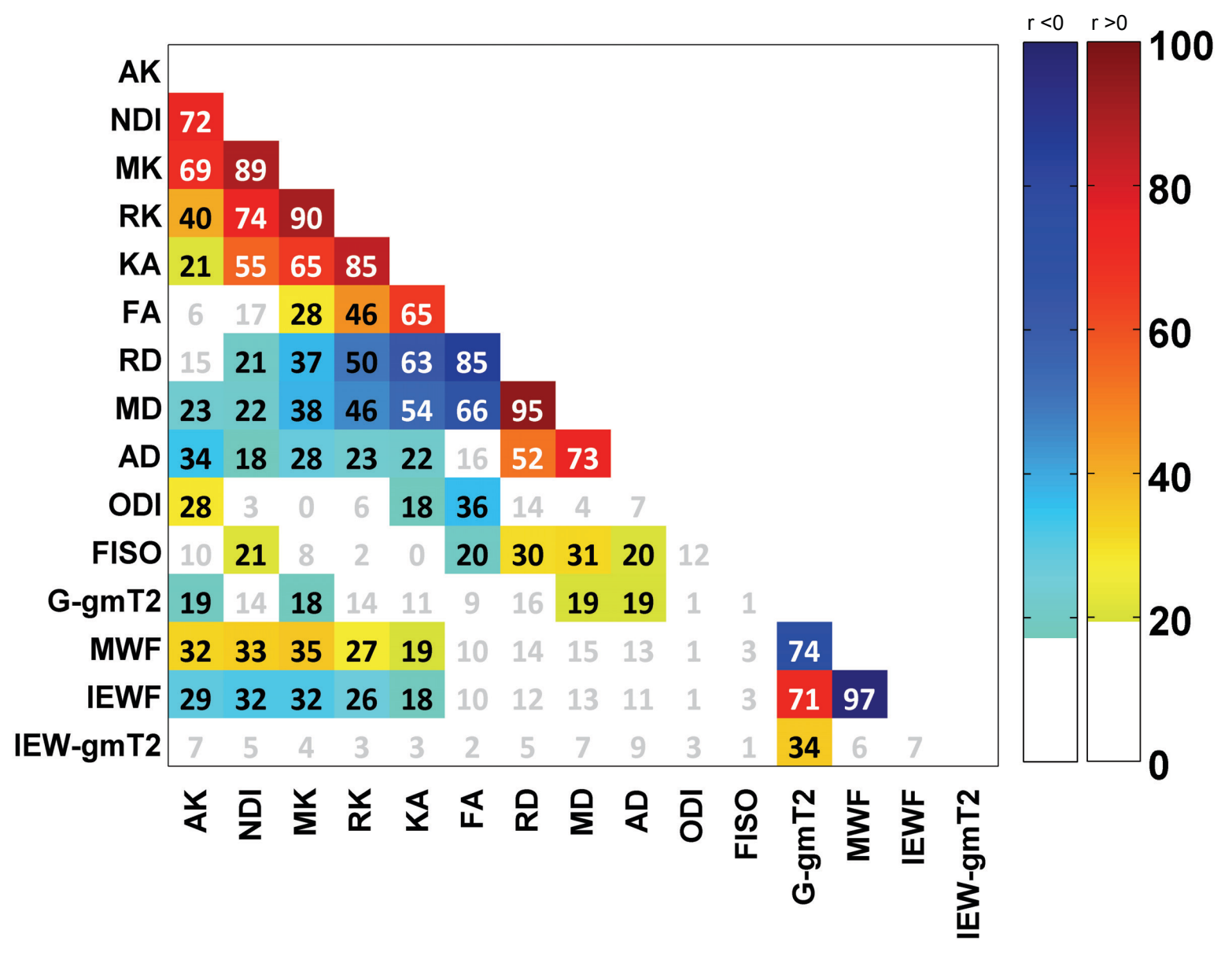
r <0
r >0
100
80
60
40
20
0
AK
NDI 72
MK 69 89
RK 40 74 90
KA 21 55 65 85
FA 6 17 28 46 65
RD 15 21 37 50 63 85
MD 23 22 38 46 54 66 95
AD 34 18 28 23 22 16 52 73
ODI 28 3 0 6 18 36 14 4 7
FISO 10 21 8 2 0 20 30 31 20 12
G-gmT2 19 14 18 14 11 9 16 19 19 1 1
MWF 32 33 35 27 19 10 14 15 13 1 3 74
IEWF 29 32 32 26 18 10 12 13 11 1 3 71 97
IEW-gmT2 7 5 4 3 3 2 5 7 9 3 1 34 6 7
AK
NDI
MK
RK
KA
FA
RD
MD
AD
ODI
FISO
G-gmT2
MWF
IEWF
IEW-gmT2

Highlights:

- We assessed a range of advanced in vivo MRI based measures of brain microstructure in healthy volunteers between 17 and 70 years old.
- Diffusion MRI metrics, including those derived from DTI and NODDI, were more sensitive to lifespan effects than myelin water imaging in our population.
- Age-related changes in frontal white matter in mid-adulthood, may be related to an altered organization of fibers rather than altered tissue composition
- Combining measures which probe different aspects of microstructure provides novel insights into neurobiological changes over the lifespan.

Supplementary Table 1

Mean size and standard deviation of total cerebral WM and regions of interest from John Hopkins University white matter atlas (Mori, et al., 2005) after applying WM masks as described in section 2.3.3.

Region of Interest from JHU atlas	Mean ROI size in study sample (voxels)	Standard deviation (voxels)
Genu of corpus callosum	605	26
Body of corpus callosum	1150	53
Splenium of corpus callosum	1175	18
Superior cerebellar peduncle	110	5
Cerebral peduncle	420	11
Anterior limb of internal capsule	478	23
Posterior limb of internal capsule	843	0
Retrolenticular part of internal capsule	608	3
Anterior corona radiata	1634	16
Superior corona radiata	1829	6
Posterior corona radiata	868	7
Posterior thalamic radiation	901	7
Sagittal stratum (include ILF and IFOF)	447	13
External capsules	626	33
Cingulum (cingulate gyrus)	219	14
Fornix crescent/stria terminalis	128	6
Superior longitudinal fasciculus	1503	14
Total cerebral WM	34272	636

Mori, S., Wakana, S., Nagae-Poetscher, L.M., P.C.M., v.Z. 2005. MRI Atlas of Human White Matter. Elsevier.

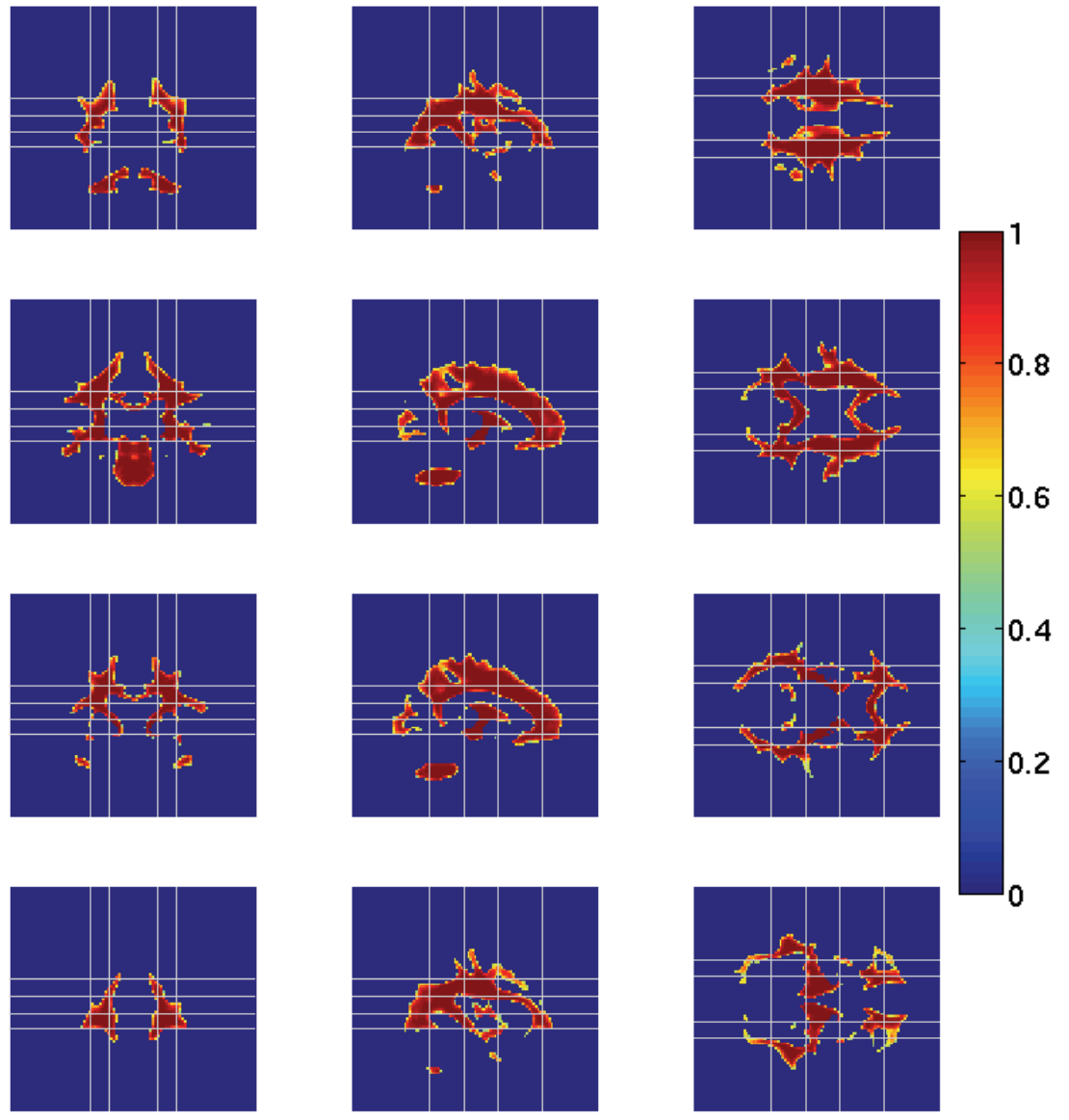
1
0.8
0.6
0.4
0.2
0

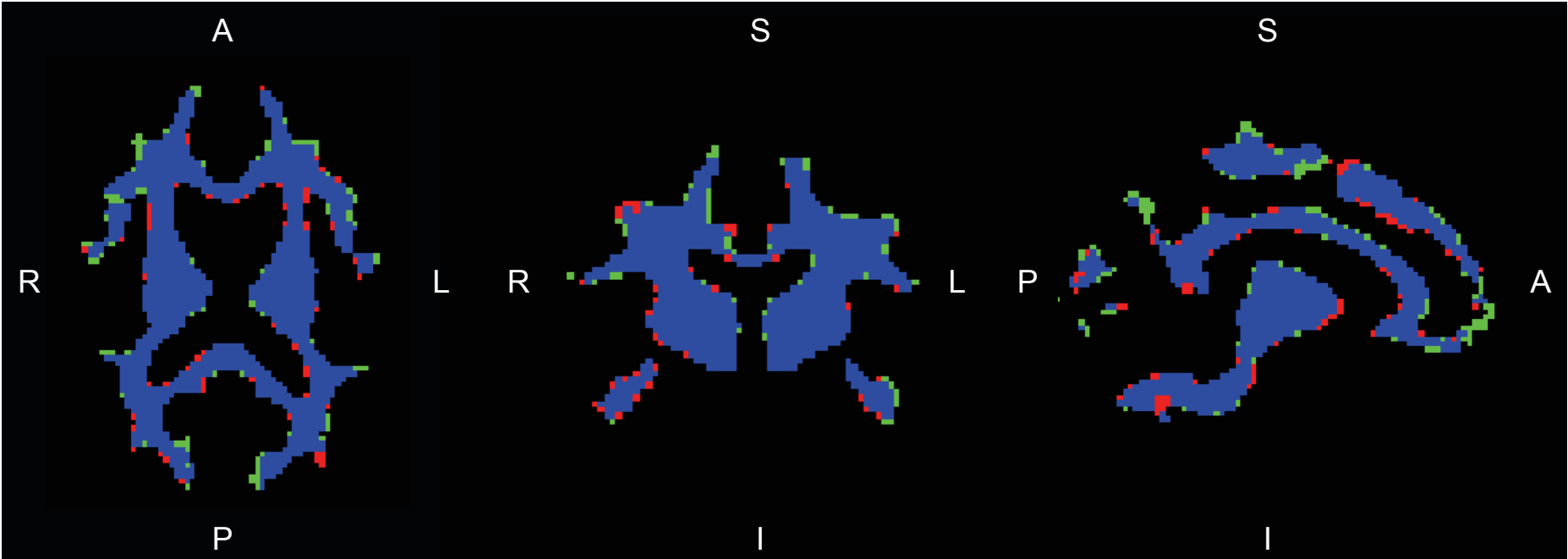
A
R
L
P
S
R
L
I
S
P
A
I
Red = youngest participants
Green = oldest participants
Blue = overlap